2020

Development and validation of a murine model for long-term intravital imaging of peripheral nerve regeneration

BOSTON UNIVERSITY

SCHOOL OF MEDICINE

Thesis

DEVELOPMENT AND VALIDATION OF A MURINE MODEL FOR LONG-TERM INTRAVITAL IMAGING OF PERIPHERAL NERVE REGENERATION

by

ROHITH M. BHETHANABOTLA

B.S., Johns Hopkins University, 2018

Submitted in partial fulfillment of the

requirements for the degree of

Master of Science

2020

Approved by

First Reader _____

Vickery Trinkaus-Randall, Ph.D.
Professor of Ophthalmology and Biochemistry

Second Reader _____

Nate Jowett, M.D.
Assistant Professor of Otolaryngology-Head and Neck Surgery
Harvard Medical School

ACKNOWLEDGMENTS

I would like to thank my mentor, Dr. Nate Jowett, as well as my research team members, Dr. Iván Coto Hernández and Steven Minderler at the Surgical Photonics Engineering Laboratory at Massachusetts Eye and Ear, Dr. Wenlong Yang at the Center for Advanced Imaging at Harvard University, and the Department of Otolaryngology-Head and Neck Surgery at Harvard Medical School for the opportunity to conduct this research. This study is supported in part by the by the Berthiaume Family Foundation and the Charles H. Hood Foundation.

DEVELOPMENT AND VALIDATION OF A MURINE MODEL FOR LONG-TERM INTRAVITAL IMAGING OF PERIPHERAL NERVE REGENERATION

ROHITH M. BHETHANABOTLA

ABSTRACT

INTRODUCTION:

Injury to the facial nerve can lead to functional and aesthetic sequelae in patients. Though surgical interventions are available to restore lost motor and sensory function, outcomes are often suboptimal due to inadequate or disorganized axonal regeneration. While engineering improvements to the standard of care are underway, gaps remain in our molecular understanding of peripheral nerve injury to translate these efforts clinically. Over the last few decades, advancements in intravital imaging such as the development of fluorescent reporter mice and use of multiphoton excitation techniques have allowed for markedly enhanced characterization of biological phenomena at higher resolutions, at greater depths, and for longer timescales. Challenges in reliably and serially imaging *in vivo* within murine models have been overcome through the development of chronic imaging windows in various settings of the body. However, there are very few techniques available presently for imaging the peripheral nerve microenvironment and no prior work detailing use in the facial nerve setting.

OBJECTIVE:

Longitudinal studies employing intravital imaging techniques carry potential to improve understanding of peripheral nerve regeneration and function. Using multiphoton microscopy and fluorescent reporter mice, we propose a prototype, surgical protocol of implantation, and initial safety and efficacy testing of a facial nerve window to enable chronic imaging for enhanced characterization of the peripheral nerve microenvironment.

METHODS:

A stainless-steel implant with an affixed glass coverslip and aluminum external fixation component was developed for implantation in a transgenic reporter mouse model to enable chronic intravital imaging of the facial nerve buccal and marginal mandibular branches. A qualitative observational study and clinical assessment scoring study was performed post-surgical implantation to monitor behavior, physical appearance, weight loss, and reactivity to animal handling over the typical time-course of nerve regeneration. Segments of facial nerve branches were harvested from control and window-implanted mice and imaged using widefield epifluorescence microscopy for axon quantification to determine any adverse effects from window compression onto axonal fibers. Two-photon microscopy (2PM) and Simulated Raman Scattering (SRS) were also performed through the window to visualize axon tracts, myelin sheaths, and surrounding collagen matrix in wild-type and transgenic mice models.

RESULTS: Qualitative serial observational studies and assessment scoring indicated no obvious functional deficits over the time-course of typical nerve regeneration and normal scores for weight, behavior, physical appearance, and reactivity. Neural histomorphometric analysis indicated no significant difference in mean myelinated axon count of buccal (mean ± SD; control buccal, 947.6 ± 129.9; window-implanted buccal, 799.3 ± 128.6; p = .136) and marginal mandibular branches (control marginal mandibular, 801.3 ± 145.1; window-implanted marginal mandibular, 738.0 ± 197.2; p = .599) between control and window-implanted mice, suggesting that neuropathy was not induced from the window itself. High-resolution images of nerve morphology in healthy and injured transgenic and wild-type mice were obtained using 2PM and SRS.

CONCLUSION: Herein, we describe a novel and replicable platform for longitudinal intravital imaging of murine facial nerve. Future studies will evaluate viability of this model for imaging the facial nerve microenvironment, particularly Schwann cell-axon interactions, in the setting of severe nerve injury over a period of several weeks to months. Improved understanding gained through such studies of the structural peripheral nerve microenvironment may allow for advancements in viral vector therapeutics, nerve graft scaffold design, as well as advanced injury diagnostics and tracking.

TABLE OF CONTENTS

LIST OF FIGURES

LIST OF ABBREVIATIONS

CARS .....Coherent anti-Stokes Raman Scattering

CNS .....Central Nervous System

C57 .....C57BL/6J Mouse Strain

FNW.....Facial Nerve Window

FP .....Facial Paralysis

IVM.....Intravital Microscopy

MPM..... Multiphoton Microscopy

PNS..... Peripheral Nervous System

SC .....Schwann Cell

SHG ..... Second-Harmonic Generation

SRS..... Stimulated Raman Scattering

Thy1-YFP..... B6.Cg-Tg(Thy1-YFP)16Jrs/J Mouse Strain

YFP .....Yellow-Fluorescent Protein

2PM..... Two-Photon Microscopy

INTRODUCTION

Introduction to Facial Paralysis

Our human ability to make facial expressions plays an integral role in conveying emotions and communicating our identity to those around us (Frith, 2009). However, when these functions are diminished as they are in patients with facial paralysis (FP), the psychosocial penalties can be devastating. Aside from nonverbal communication, FP can affect vital functions such as blinking, corneal protection, lacrimation, nasal breathing, speech articulation, and taste. These all occur through the recruitment of facial musculature, innervated by the facial nerve and its branches (Jackson & von Doersten, 1999).

Several studies have previously demonstrated the link between loss of facial animation in patients and psychological distress (Macgregor, 1990). Patients with FP tend to report higher depression scores, lower self-rated attractiveness, and lower quality of life (Nellis et al., 2017). Studies have also shown the social challenges associated with managing FP. In a study done by Li and colleagues in 2016, random observers rated pictures of patients with FP negatively on scales of attractiveness, trustworthiness, and intelligence (Li et al., 2016). However, when corrective surgery was performed in patients with severe facial paralysis, observers rated patients with greater attractiveness and improved affect display (J. Dey et al., 2014; J. K. Dey et al., 2014). At the same time, Ryzenman and colleagues found that despite having some form of treatment for acoustic neuroma surgery, 28% of patients continued to express

discontent with their condition (Ryzenman et al., 2005). These results have several implications that set up the importance of clinical management of facial paralysis: (1) impaired facial expression carries psychosocial penalties when untreated, (2) treatment in patients can improve societal perceptions surrounding FP, and (3) there is an underserved need to improve the standard of care to allow patients to regain important daily function and feel a greater sense of comfort in society after treatment (Ishii et al., 2018).

Clinical Care for Facial Paralysis

The facial nerve is a mixed nerve that contains general somatic afferent (sensory from external acoustic meatus and deeper parts of the auricle), special afferent function (taste from anterior two-thirds of tongue), general visceral afferent (lacrimal gland, submandibular and sublingual salivary glands, and nasal cavity mucous membranes), and branchial efferent (superficial facial muscles, stylohyoid, and posterior belly of digastric muscles) functions (Standring & Gray, 2008). Impairment of the nuclei or the fibers can result in partial or complete facial paralysis. Causes of FP can stem from infectious, neoplastic, developmental, iatrogenic, idiopathic, and traumatic reasons (Owusu et al., 2018). Because of varied etiologies, it is crucial that clinicians understand the cause, progression, and duration of injury and perform a thorough head and neck examination, cranial nerve examination, and otoscopy to establish a diagnosis (Jowett, 2018). Electrophysiologic studies can also be used to determine the

integrity of the facial nerve by assessing the ensuing motor response after stimulus (Owusu et al., 2018). Based on the findings from the historical and physical examination, an assessment about the severity of injury and potential for functional recovery classification is determined to develop an appropriate therapeutic strategy.

Based on the descriptions of nerve injury stages from Seddon in 1943 and Sunderland in 1978 along with the grading scale proposed by House and Brackmann in 1985, clinicians are able to predict prognoses on a 5-point scale (Seddon, 1943; Sunderland, 1978). Grade I nerve injury, known as neuropraxia, is a reversible and temporary block of conduction where some axonal abnormalities might exist, but complete recovery is expected. Grade II nerve injury, known as axonotmesis, is where some Wallerian degeneration occurs distal to the injury site, but recovery is fully expected with possible facial weakness because endoneurial tubes formed by the Schwann cell basal lamina are still intact (Brushart, 2011). Grade III nerve injury, known as neurotmesis, occurs when there is loss of axonal and myelin tubes. The endoneurium can be disrupted with intra-fascicular fibrotic scarring present ultimately affecting functional recovery outcomes. Grade IV and Grade V nerve injuries refer to partial or complete transection of a nerve which will lead to minimal facial function or complete loss of functional recovery respectively (Jackson & von Doersten, 1999). Once severity is classified, the clinician may consider surgical options or non-surgical options such as physical therapy and denervation agents.

For patients with severe FP where the facial nerve is transected or facial musculature is absent, surgery is automatically considered. Where there exists potential for spontaneous recovery of facial function following neural insult, patients are closely observed for several months before resorting to surgical intervention.

The main goal in surgical reanimation is to guide regenerating nerves to their distal targets to maximize the likelihood of target innervation (Gelberman, 1992). Reanimation procedures are either static, in that they improve facial resting symmetry without restoring motion, or dynamic, in that they restore functional movements. Typically, a combination of procedures is employed to optimize functional and aesthetic results. One method of repair is through a direct neural coaptation procedures known as neurorrhaphy, where proximal and distal nerve stumps are opposed and secured together using microsutures. Difficulties with this procedure include aligning the nerve fascicles together without inducing any tension. If large gaps exist between a proximal nerve stump and its distal target, another method called interposition nerve grafting is required to guide and support regenerating axons along the gap. This involves harvest of a less-critical sensory nerve autograft from an alternate site such as the lower leg. Nerve autografts provide a Schwann cell-rich scaffold to support axon regeneration, but their harvest results in sensory loss at the donor site, necessitates a secondary operating site, and carries risk of long-term donor site pain development (Radtke & Kocsis, 2014). Furthermore, availability of sufficient autograft nerve length can

be problematic in young children and in cases where extensive limb trauma is present. Extensive tissue engineering research is underway to develop new materials for artificial conduits, but limitations regarding size of conduits has limited its clinical adoption thus far (Pfister et al., 2011). A third technique, nerve allografting, is typically only reserved for the most severe nerve injuries and carry risk of host immunosuppression even though steps may be carefully taken to suppress this (Ray & Mackinnon, 2010). Where the facial musculature has been denervated for periods in excess of one year, functional muscle transfer is recommended for dynamic reanimation. This involves harvest of a muscle from a distant site together with its neurovascular pedicle, revascularization, and nerve coaptation to donor nerves in the face, followed by meticulous inset of the muscle fibers to facial landmarks to reestablish desired facial movements. The gracilis muscle, for example, is most often used for smile restoration (Jowett & Hadlock, 2018). Following dynamic reanimation procedures, post-operative physical rehabilitation techniques are employed to optimize the surgical result.

Pathophysiology of Facial Paralysis

To best understand the pathology and the efforts to make advancements in the care for facial paralysis, a brief description of general nervous system anatomy followed by nerve histology is necessary.

The human nervous system is anatomically organized into two major divisions: the central nervous system (CNS) and the peripheral nervous system

(PNS). The CNS consists of the brain and spinal cord, while the PNS is composed of the cranial, spinal, and peripheral nerves that allow impulses to and from the CNS. In both systems, cells are either classified as neurons, which have the main function of transmitting electrical signals, or glial cells, which have supportive roles such as providing nutrition to neurons, acting as a means of defense for neurons, or promoting local neuronal activity. When changes in the local environment of a neuron occur, impulses are sent from the cell body to dendrites via the axon. Peripheral axons can differ in morphology depending on function. In the PNS, glial cells called Schwann cells (SCs) form myelin around axon segments (Brushart, 2011). Composed of cholesterol and sphingolipids, the myelin sheath encircles the axon and forms layers as the SC elongates. Myelin reduces the capacitance of the axonal membrane allowing conduction of the impulse along the axon at each node of Ranvier. Without myelin, conduction velocity would be greatly diminished, thus interfering with normal action potential generation and propagation (Mescher, 2018).

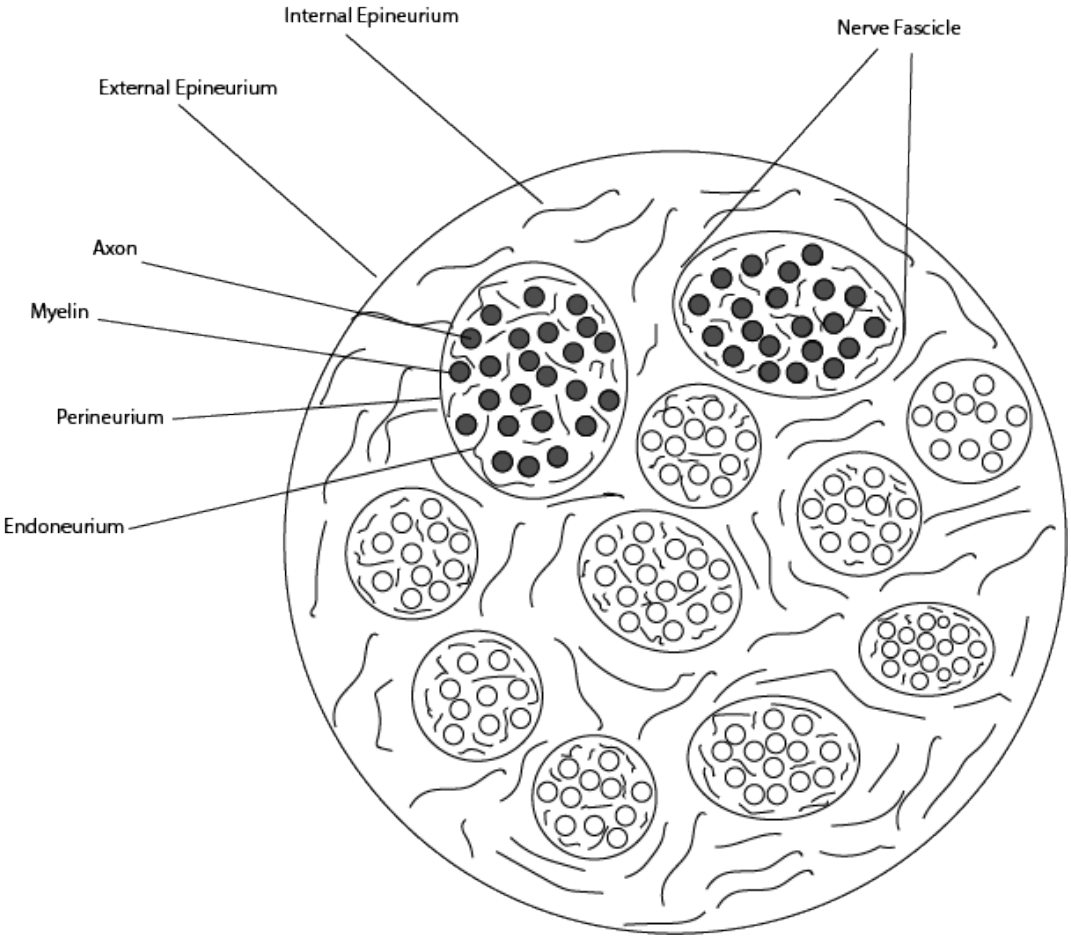

Figure 1. General cross-section of a normal peripheral nerve along with its connective tissue components. Not shown here is the relative density of collagen fibers in each layer and mesoneurium surrounding nerve.

The structure of a motor nerve is described in **Figure 1**. When peripheral axons are enclosed by connective tissue, they form the general organization of nerves. The epineurium encloses the peripheral nerve and is composed of primarily type I collagen and type III collagen (Millesi & Terzis, 1983; Salonen et al., 1985). It also contains elastic fibers (Thomas, 1963). The main function of the epineurium appears to be maintenance of nerve integrity upon elongation and

protection for nerve fascicles (Rydevik et al., 1990). The perineurium is the layer that defines a nerve fascicle. It is composed primarily of type III collagen and has the main function of serving as a blood-nerve barrier allowing vascularization to support the neurons within the endoneurium, the innermost layer that surrounds individual axons (Lorimier et al., 1992). Composed of a mixture of collagenous fibers, the endoneurium also contains resident macrophages and matrices rich with glycoproteins and proteoglycans that play a key role in the nerve regeneration process after injury. The basal lamina is a thin layer of extracellular matrix that anchors SCs and ensures axons are myelinated properly (Chernousov & Carey, 2000). The interaction between axons and its SCs plays a key role in axon regeneration because the complex determines how many SCs are needed to myelinate a given axon, how thick that myelin should be to propagate the signal, and the length of myelination which ultimately determines the spacing of the nodes of Ranvier (Brushart, 2011). The diagram in **Figure 2** describes the interaction in further detail.

Facial nerve injury falls under a larger category of PNS injuries that have been extensively studied alongside CNS injuries in animal models, where nerve compression, crush, or transection are administered to understand the mechanisms of injury and axon regeneration. Due to the inhibitory environment of the CNS, such as glial scars affecting axonal outgrowth or slower myelin debris clearance as compared to the PNS, nerve regeneration is thought to occur with less impediment in the PNS than the CNS (He & Koprivica, 2004; Vargas &

Barres, 2007). Clinically, it has been shown that patients recover best when injuries are distal as opposed to proximal, when injuries occur in younger patients versus older patients due to the shorter distance needed to travel to target tissue, and when nerve injuries fall under Sunderland I-III type injuries versus Sunderland IV or V (Sunderland, 1978; Brushart, 2011). In studying these trends, the cellular mechanisms behind nerve regeneration have become further elucidated in animal models. For meaningful nerve regeneration to occur, axons must have a distal environment supportive of regrowth, a target site amenable for accepting new axons, and the growth factors necessary to support regeneration (Scheib & Höke, 2013).

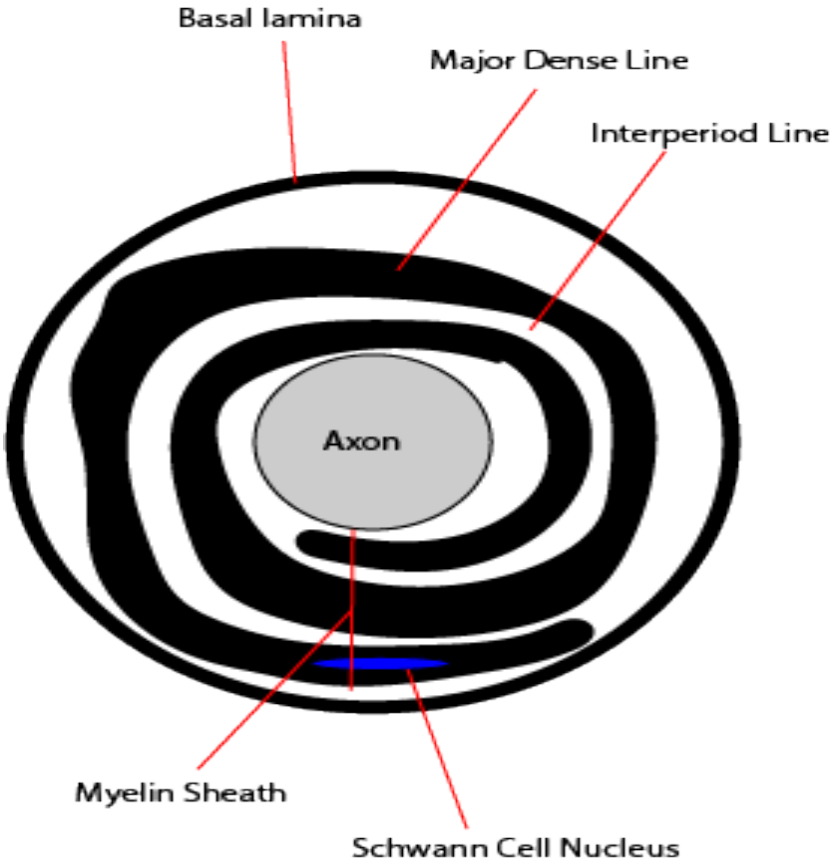

Figure 2. Cross-sectional illustration showing the myelination of PNS axons and the relationship between axon and myelinating Schwann cells. PNS axons are engulfed by Schwann cells that fuse around the axon. The fused membrane wraps itself around the axon as the Schwann cell moves around it many times. This circumferential wrapping pattern forms the myelin sheath. The major dense line is intracellular and the inter-period line is extracellular.

Translation of mechanistic discoveries in the field of peripheral nerve regeneration in murine models to meaningful clinical therapies has heretofore remained slow. Currently, the use of murine models have been justified as an inexpensive source of mammalian nervous tissue and as having indistinguishable morphology when compared to the human nerve (Bridge et al.,

1994; Mackinnon et al., 1985). However due to the inherent size differences of rodents versus humans, axons in humans are required to travel much longer distances than in mice which therefore leaves them susceptible to environments of chronic denervation. This is characterized by atrophied Schwann cells, reduced expression of neurotrophic factors, loss of basal lamina to guide growth, among other reasons. Furthermore, because of the extended distances of vesicular transport along the axons in humans, it has been shown that regeneration occurs at about 1 mm/day in humans versus 3 mm/day in rodents (Gutmann et al., 1942; Holmquist et al., 1993). While solutions therefore may be suitable for injury in animal models, they have not been shown yet to belong in the standard of care for humans. To solve this issue, rodent models of chronic denervation of over 10 weeks have been proposed as they may serve as better models to capture the situation in humans (Gutmann et al., 1942; Holmquist et al., 1993).

When injury occurs, the neuronal cell body undergoes chromatolysis, a process that includes swelling of the cell body, movement of the nucleus, and dissolution of Nissl bodies (Lieberman, 1971). The effect of this is downstream gene expression changes, particularly the downregulation of neurofilament that sustains axon diameter. Meanwhile, the upregulation of actin and myosin allow the filopodia from the proximal nerve stumps to move in search of distal targets (Fu & Gordon, 1997). The distal nerve stump undergoes Wallerian degeneration where myelin is broken down followed by proliferation of Schwann cells. SCs

form bands of Büngner which interact with regenerating axons to guide them. Infiltrating macrophages clean up inhibitory debris to facilitate this process. In instances where chronic denervation of over 10 weeks occurs, the Schwann cells atrophy resulting in the subsequent deterioration of basal lamina tubes for axons to follow (Ide & Kato, 1990; Scheib & Höke, 2013). This creates an environment unsuitable for regeneration of axons and the muscle fibers begin to decrease in number and size as well due to lack of innervation (Anzil & Wernig, 1989). Because human nerves need more time for target innervation as compared to murine models for aforementioned reasons of slower growth rates and longer distances that need to be traveled, the risk of chronic axotomy and denervation requires the use of accurate diagnosis methods and timely surgical intervention to increase the likelihood for regeneration and subsequent functional outcome.

Experimental Studies in Peripheral Nerve Regeneration

Experimental solutions have been discovered to overcome the effects of chronic axotomy by increasing neuron survival, accelerating the expression of neurotrophic factors, attempting to prevent neuronal apoptosis, improving axon regeneration by activating dormant Schwann cells or by preventing Schwann cell atrophy with scaffold material (Scheib and Hoke, 2013). On the engineering side, solutions have been also developed such as tissue-engineered nerve grafts and improved diagnostic methods for detecting severity of injury, but these have yet become the standard of care because of knowledge gaps in our understanding of

molecular mechanisms behind SC role in nerve grafts and axonal behavior (Pfister, 2011). To further understand these mechanisms, we propose herein the use of intravital imaging by multiphoton microscopy in a transgenic fluorescent reporter mice model of facial nerve injury.

Conventional assessment of tissue at the micro-scale level employs tissue harvest, fixation, and histological processing for microscopic analysis. Conventional imaging techniques involve the use of single-photon visible light absorption processes for contrast generation, effectively limiting the potential imaging depths to 100 μm or less from the surface of the tissue section (Helmchen and Denk, 2005). Furthermore, conventional imaging techniques are static in nature (i.e., at a single time-point at time of tissue harvest) which restricts a deeper understanding about the dynamic nature of biological phenomena. More recently, particularly in the last two decades, imaging of living tissue at subcellular resolution, otherwise known as intravital multiphoton microscopy (IVM), has allowed for the identification of causal relationships, confirmation of the sequential order of events that occur in various processes, and discovery of the interactions between cells in three physical dimensions longitudinally in time (Misgeld and Kerschensteiner, 2006). Biologists are now able to understand cellular behavior in vivo at greater depths, for longer time intervals, over larger tissue areas, and at resolutions that were previously impossible to achieve (Pittet and Weissleder, 2011).

IVM works by exciting fluorescence in a given tissue, collecting light emitted from it, and separating the out-of-focus light from the signal without inducing any photodamage to tissue. In conventional one-photon microscopy, contrast generation involves a single photon that depends linearly on incident light intensity. Multiphoton microscopy, however, uses “non-linear” excitation to excite fluorescence within a focal plane. In 1931, Maria Göppert-Mayer demonstrated the possibility of photons of lesser energy to cause an excitation equivalent or greater than the absorption of a single higher energy photon when simultaneously absorbed (Göppert-Mayer, 1931). In two-photon microscopy (2PM), short pulses of laser light on the order of the 10^{-15} s are employed to excite a fluorescence molecule via the simultaneous absorption of two photons. This occurs as a quadratic dependence on the intensity as opposed the linear intensity dependence of single-photon excitation techniques (Zipfel et al., 2003). A comparison between one-photon versus two-photon is shown in **Figure 3.**

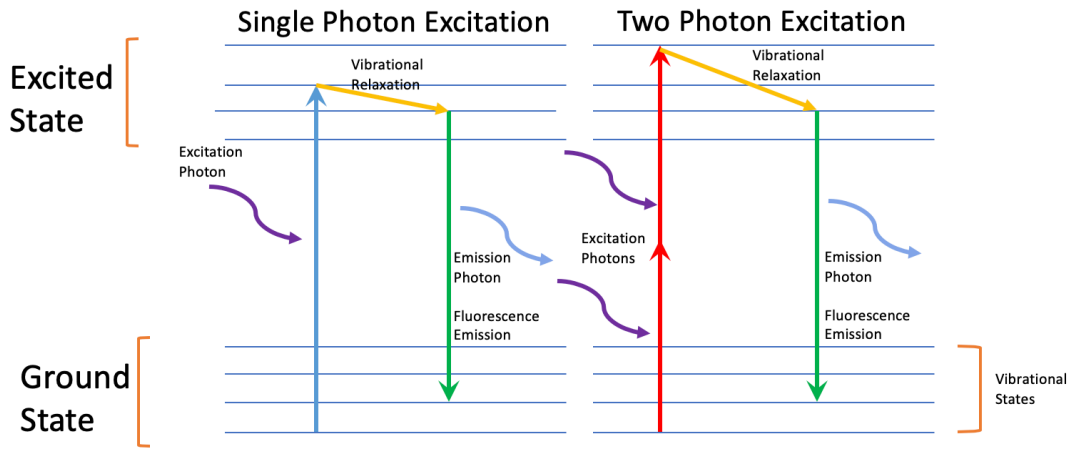

Figure 3. Jablonski diagram describing single-photon and two-photon excitation principles. The absorption of the energy of one excitation photon (via UV or visible light) excites fluorescent molecules and induces a transition from ground to excited electronic state *(left)*. This same transition can be excited with two less energetic photons through intermediate states that are simultaneously absorbed *(right).*

MPM has been utilized extensively over the last two decades to study angiogenesis, lymphocyte trafficking, embryonic development, and metastasis (McDonald & Choyke, 2003; Wang et al., 2002; Miller et al., 2002; Squirrell et al., 1999). It has been used in studying neurodegenerative disease, ischemia, inflammation, and neuronal plasticity (Kawakami et al., 2005; Svoboda et al., 1996; Brendza et al., 2005; Iadecola, 2004). Multiphoton excitation microscopy has several advantages over single-photon technique. Typically, less photobleaching and damage to biological tissues in the focal plane is observed using MPM when compared to single-photon laser fluorescence techniques such as confocal imaging. MPM also permits for imaging at greater tissue depths in

comparison to single-photon techniques (several hundred microns as opposed to 100 microns or less). Furthermore, because there is expanded wavelength accessibility of fluorophores, multicolor imaging is made simpler and chromatic aberrations are more readily avoided (Zipfel et al., 2003).

Though MPM is a useful technique for deep imaging of samples having fluorescent labels, such labelling is often unfeasible in vivo. MPM systems can also be used to resolve sub-cellular structures using non-fluorescent processes. Second-harmonic generation (SHG) is one such process, wherein two incident photons of a particular wavelength merge into a single photon of half the wavelength following interaction with a non-linear material (Pittet and Weissleder, 2011) without molecular excitation. For SHG to occur, molecules of the material must be inversion-asymmetric and spatially ordered. In biologic tissue, collagen and microtubule orientations are suitable for investigation using SHG microscopy (Helmchen and Denk, 2005).

MPM may also be employed in label-free vibrational imaging of tissue. Stimulated Raman scattering (SRS) and coherent anti-Stokes Raman scattering (CARS) have been utilized to provide information on the vibration frequencies of characteristic chemical bonds such as in lipids, nucleic acids, or proteins (Wei et al., 2013; Freudiger et al., 2008; Zhang et al.; 2013). Spontaneous Raman scattering imaging is limited in use due to having weak signals which necessitates a long integration time to achieve a good signal-to-noise ratio (Zhang et al., 2013). Therefore, it is not ideal for live-cell imaging as biological

phenomena often occur within short time scales. CARS is one method to improve speed of imaging, however, this suffers from non-resonant background and distortion, among other issues (Wei et al., 2013). SRS has emerged as a better candidate with its improved signal-to-noise ratio and linear proportionality to target molecule concentration which allows for easier chemical contrast interpretation (Freudiger et al., 2008). Briefly, SRS works when two focused beams of lasers are simultaneously overlapped spatially and temporally. The difference in energies of the pump and Stokes lasers are set to match the frequencies of the desired molecules that are to be imaged. In the case of myelin, the frequency difference is selected to excite the resonance of CH2 stretch mode found in lipids. Put together, the use of SRS and CARS has greatly enhanced imaging of the nervous system as the techniques have been used in models of nerve injury and amyotrophic lateral sclerosis (Henry et al., 2009; Tian et al., 2016). Jablonski diagrams comparing the processes of 2PM, SHG, SRS, and CARS are depicted below in **Figure 4.**

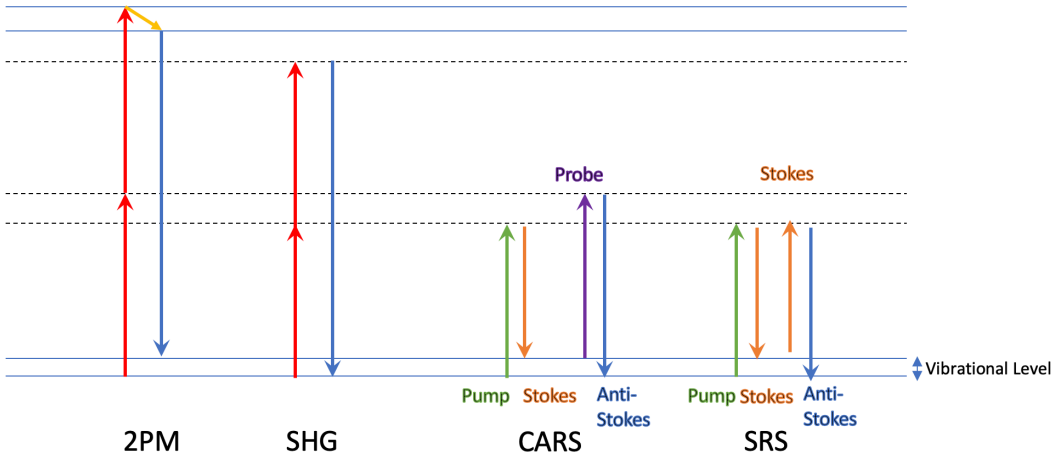

Figure 4. Jablonski diagram illustrating 2PM, SHG, CARS, and SRS.

Aside from imaging techniques, the advent of new fluorescent probes in IVM to generate contrast must be noted. Some fluorescent probes are able to be genetically encoded, while some are dyes that are used to stain cells ex vivo. Some probes are able to be directly injected into the animal for visualization of structures or cellular activities. The development of transgenic mice that express fluorescence at high levels in neurons has been particularly useful to advance understanding of mammalian neurobiology (Feng et al., 2000). In the study by Feng et al. in 2000, peripheral and central neurons of mice were successfully labelled with various spectral variants of green fluorescent protein (designated 'XFPs'), all under the control of common regulatory elements from the Thy1 gene. Presumably because of a phenomenon called position effect variegation, XFPs were expressed in unique patterns where some neuronal subsets were more intensely labelled compared to others. These findings have paved the way for studies involving specific labelling of neuronal subtypes and various

components of the neuron such as axons, synaptic terminals, or dendrites (Keller-Peck et al., 2001; Lee et al., 2005).

Equipped with enhanced microscopy techniques and fluorescent proteins for intravital imaging, the challenge then becomes to develop the appropriate surgical techniques and necessary hardware for longitudinal studies to help elucidate the dynamics of axonal regeneration. In the last two decades, several studies have sought to solve this problem through the use of “imaging windows” or “imaging chambers.” Cranial imaging windows have been readily used to investigate neurovasculature and other phenomena (Holtmaat et al., 2009; Koletar et al., 2019; Kienast et al., 2010; Pan et al., 2008, Heo et al., 2016). Spinal cord chambers have been described for imaging injury pathology (Farrar et al., 2012). A mammary window was developed to investigate metastatic tumors (Kedrin et al., 2008). A dorsal skin-fold chamber was developed to image subcutaneous tumor formation (Lehr et al., 1993). More recently, a chronic longitudinal window was developed to image metastatic lesions in lymph nodes (Meijer et al., 2017). These windows were used to avoid surgical opening of the animal for each imaging time point which would otherwise add confounding variables such as potential risk of infection, inflammation, tissue damage, as well as pain and distress to the animal. Despite the abundance of protocols detailing use of imaging windows, there has been a paucity of studies documenting peripheral nerve function. Brodnick et al. in 2014 details the use of a peripheral nerve window for sciatic nerve imaging and Grochmal et al. in 2019 describes

use for a tibial nerve window (Brodnick et al., 2014; Grochmal et al., 2018). The need becomes clear, therefore, to develop a “window” through which continual optical access is possible to image the facial nerve microenvironment during the entire course of injury, only limited by how often the animal can tolerate being restrained or placed under general anesthesia. There is no prior published work characterizing use of an optical window to image facial nerve pathology, especially in the setting of nerve injury and regeneration. Herein we characterize the development and initial validation of a facial nerve window (FNW) drawing from previously characterized optical windows for longitudinal imaging of tissue in living animals.

Specific Aims

Injury to peripheral nerves can have significant physical and emotional effects on patients. Though research has yielded some breakthroughs to improve surgical management, clinical outcomes are not without a myriad of risks and carry significant rates of failure for certain procedures. The aim of this research is to leverage recent developments in intravital imaging paired with the development of a novel implantable device to facilitate long-term characterization of facial nerve regeneration in a transgenic murine model. This research carries potential to help advance development of novel therapies to improve clinical outcomes for patients with peripheral nerve disorders. Herein, we describe a replicable, low-cost facial nerve window device together with surgical

implantation procedure for serial intravital imaging of the facial nerve microenvironment over a timescale relevant to nerve regeneration that obviates the need for repeated surgical procedures in transgenic and wild-type mouse models. The aims are as follows:

1) Design a low-cost, biocompatible tool for chronic imaging of the buccal and marginal mandibular branches of the murine facial nerve.
2) Develop a surgical preparation, implantation, and post-operative standard operating procedure for chronic imaging of the buccal and marginal mandibular branches of the murine facial nerve.
3) Verify that such a tool can be tolerated without any induced pathology over the typical time-course of murine facial nerve regeneration.
4) Verify whether this approach and device induces any obvious functional or histological changes in the facial nerve microenvironment in comparison to control animals.

METHODS

Animal Model

Transgenic mice were used in this study as models for peripheral nerve regeneration. Advancements in stain-free imaging have made it possible for transgenic strains to serve as ideal models to greatly enhance assessment of nerve regeneration. The B6.Cg-Tg(Thy1-YFP)16Jrs/J (Jackson Laboratories, Bar Harbor, ME) strain was used as these animals strongly express yellow fluorescent protein (YFP) with great specificity and at high levels in motor and sensory axons. C57B/6J (C57) (Jackson Laboratories, Bar Harbor, ME) mice were used as control mice in experiments as needed. All mice were bred in-house and co-housed in groups of five on a 12-hour/12-hour light-dark cycle with ad libitum standard feed. Animals that underwent surgery were housed separately for 1 week and monitored for recovery before being co-housed in cages.

Development and Design of Nerve Window

The design of the nerve window is shown in **Figure 5.** The stainless-steel nerve window (8.75mm x 16.75mm x 1.00mm) comprises of two holes, one through (inner diameter: 4mm; outer diameter: 6mm) and the other tapped (M2.5x0.45; outer diameter: 4.5mm). The two holes are connected by a bridging piece. The edges were filleted to avoid mice from injuring themselves or each

other when co-housed. Stainless Steel 316L was chosen as it is the most corrosion resistant when in contact with biological fluids, minimizes likelihood of infection, and is cost-effective (Disegi & Eschbach, 2000). The design was developed using Fusion 360 (Autodesk, USA) and manufactured using a commercial computer numerical control milling service (eMachineShop, Mahwah, NJ).

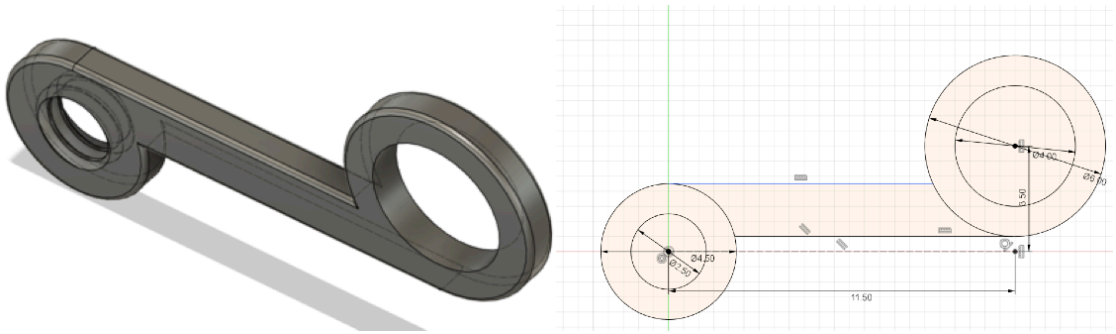

Figure 5. Current 3D iteration of the nerve window *(left)* along with dimension schematics *(right)*. Thickness dimensions of the window (1mm) are not shown.

A ring of cyanoacrylate glue (Loctite, Germany) was applied onto the outer edge of the 6mm ring and an 8mm diameter glass cover slip was affixed concentrically. A cross-sectional rendering of implantation is described below in **Figure 6.**

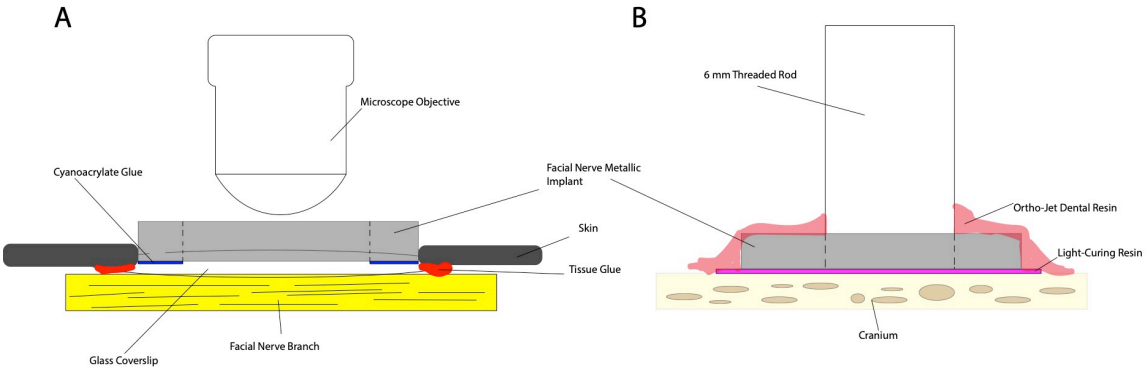

Figure 6. Cross-sectional rendering describing the implantation procedure. (A) describes the placement of the coverslip onto the nerve branch of interest. Ethyl-2-cyanoacrylate glue (Loctite) is used to affix the coverslip to the metallic implant while *n*-butyl-cyanoacrylate tissue glue (VetBond) is used to glue to the skin onto the coverslip. **(B)** describes the anchoring of the implant onto the cranium of the mouse head using two resins for proper cementation. A 6mm-long, 2.5mm diameter rod is threaded into the tapped hole. Images are not to scale.

The nerve-window is then bent such that the two holes are orthogonal to each other to roughly reflect the curvature of the mouse skull. The dimensions of the nerve window were determined by measuring distances between facial landmarks on several adult mice. For the purposes of visualization under our two-photon laser scanning system (TrimScope, LaVision BioTec, Germany), several accompanying fixtures were developed and utilized to spatially position the mouse head precisely and consistently across test subjects. A 2.5mm diameter, 6mm length threaded rod (McMaster Carr, Elmhurst, IL) was inserted into the tapped hole of the nerve window atop the mouse head and attached on the other end to an aluminum-built specialized part shown in **Figure 7** that is mounted onto a large dual-axis goniometer (ThorLabs, Newton, NJ). The

goniometer allows for rotation of the mouse head to a desired angle. The entire system is attached to a linear rail to position the nerve window translationally under the microscope objective. The microscope stage itself had positioning capability in XYZ axes and was primarily used to bring the mouse axially from the objective plane. **Figure 8** shows a diagram of the entire set-up along with associated engineering drawings.

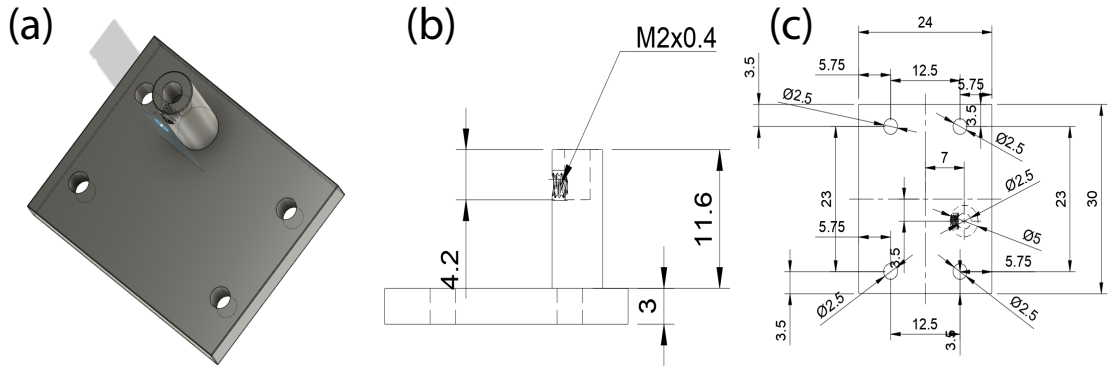

Figure 7. Current 3D iteration of goniometer external fixation component along with dimensional schematics. (a) shows an isometric 3D image of the plate built to be affixed onto the goniometer. The cylindrical hole is for receiving the 2.5 cm threaded rod attached onto the rat. The threaded hole is meant to tighten the rod in place using a M2 screw. **(b)** shows the side profile dimensions. **(c)** shows top-down dimensions.

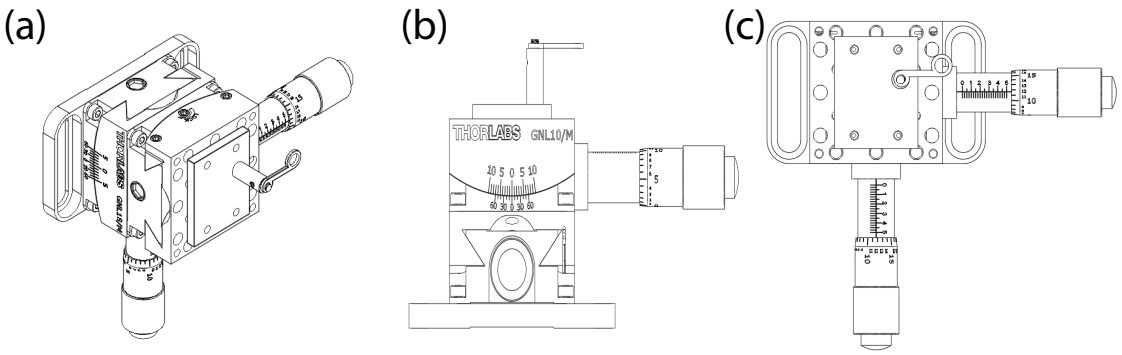

Figure 8. Assembly for Mouse Fixation under 2PM Objective. (a) shows an isometric profile of the GNL20/M goniometer (ThorLabs, Newton, NJ) with the aluminum goniometer fixture built to receive the 2.5cm rod affixed onto the rat cranium. **(b)** shows a side profile of the assembly. **(c)** shows a bird's-eye-view profile of the assembly. Not shown is the mouse itself. Diagram does not reflect the bending necessary to secure the FNW onto the mouse. See **Figure 10**.

Surgical Protocol

Surgical experiments were performed in accordance with the National Institutes of Health Guide for the Care and Use of Laboratory Animals, with Institutional Animal Care and Use Committee approval. All efforts were made to minimize the number of animals used and suffering that might occur from procedures.

Prior to operating, all surgical instruments were sterilized using autoclave or bead sterilization techniques. Each mouse was individually removed from its cage and placed into a clean induction chamber. Isoflurane (3%) was delivered in 1 L/min O_2 until sedation is noted. It was then removed from the induction chamber and placed in a left lateral decubitus position on a warming pad covered

with a sterile drape to maintain core body temperature while under anesthesia. All procedures were performed using an operative microscope (Leica Biosystems, Wetzlar, Germany). Each mouse was affixed with a nose-mask and maintained at isoflurane anesthesia (2%) in 1 L/min O_2. Buprenorphine (0.1 mg/kg) and meloxicam (1.0 mg/kg) were administered subcutaneously for intraoperative analgesia prior to skin incision. Surgical sites, depending on the procedure, are then meticulously shaved. A cotton tipped applicator is used to remove any hair or debris that might occlude the surgical site. During surgery, breathing rate and reaction to toe pinch are monitored every 5 minutes to ensure the appropriate depth of anesthesia is maintained throughout. For mice that undergo facial nerve crush or transection, animals are prepped as indicated above. A 1 cm unilateral horizontal incision is made using a #15 blade scalpel under the ear to expose the main trunk of the facial nerve. For nerve transection, sharp micro-scissors are used to cut the proximal and distal ends of the main trunk. Nerve transection injuries (Sunderland type V) were used in this study as these were easier to standardize and comparisons can be made more readily compared to healthy nerves as opposed to a Sunderland type I compression injury (Wood et al., 2011).

In mice that were implanted with the nerve window device, a 1 cm horizontal incision is made using a #15 blade scalpel over the left or right cheek to expose the pes anserinus where the buccal and marginal mandibular branches of the facial nerve diverge. A rat facial nerve anatomy diagram is

depicted in **Figure 9**. Although experiments were performed on mice, this diagram describes the general facial nerve organization of mice as well.

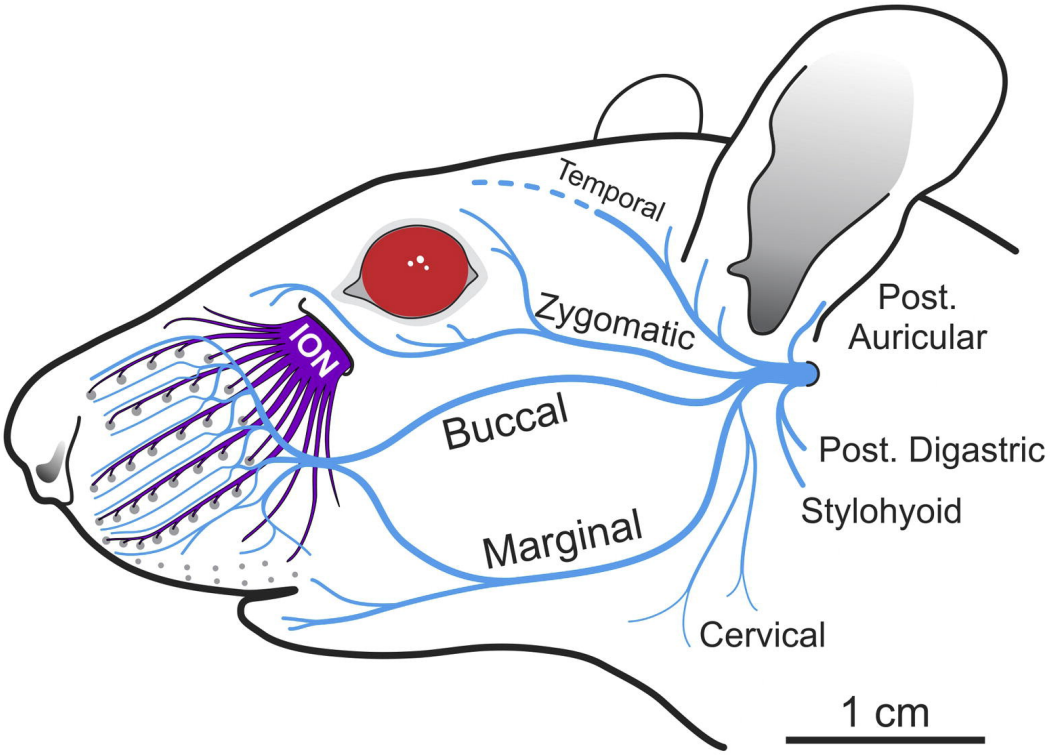

Figure 9. Diagram of a rat facial nerve branches (in blue) starting from the stylomastoid foramen cranial exit onwards. Buccal and marginal branches of the facial nerve were imaged through the glass coverslip of the facial nerve window in this study. Reprinted with permission from Heaton et al., 2014.

A second 1.5 cm incision is made in the midline sagittal plane over the cranium. Atop the cranium, local blood vessels are cauterized using metal instruments heated in a bead sterilizer to limit edematous leakage of fluid into the operating site that would prevent tight bonding of the adhesive to the bone. Over the course of the study, we found that scalpel blades, while effective in removing

aponeurotic galea, also induced micro-abrasions and bleeding in the operating site, affecting the ability for the nerve window to be secured onto the calvarium. Therefore, this was used sparingly. Once thoroughly cleaned, a base layer of Flow-It ALC Flowable Composite (Pentron Clinical, USA) is applied and cures within 2 minutes upon illumination with a 1200-2000mW LED Light (BoNew, China). A subcutaneous tunnel is developed between the two incisions, and the nerve window stainless steel 316 device is interposed between them. Alternate applications of fast, self-curing resin called Ortho-Jet Powder and Ortho-Jet Liquid (Lang Dental, USA) help to then secure the nerve window over the calvarium. Gentle pressure is applied onto the nerve window for about three minutes to promote tight bonding. The skin of the face is then secured onto the outer coverslip edge that was previously glued onto the inner frame of the implant using tissue glue (VetBond, 3M). The skin of the head is glued onto the hardened layer of resin that sits atop the skull. Pictures displaying the nerve window placed in deceased mice are shown in **Figure 10.**

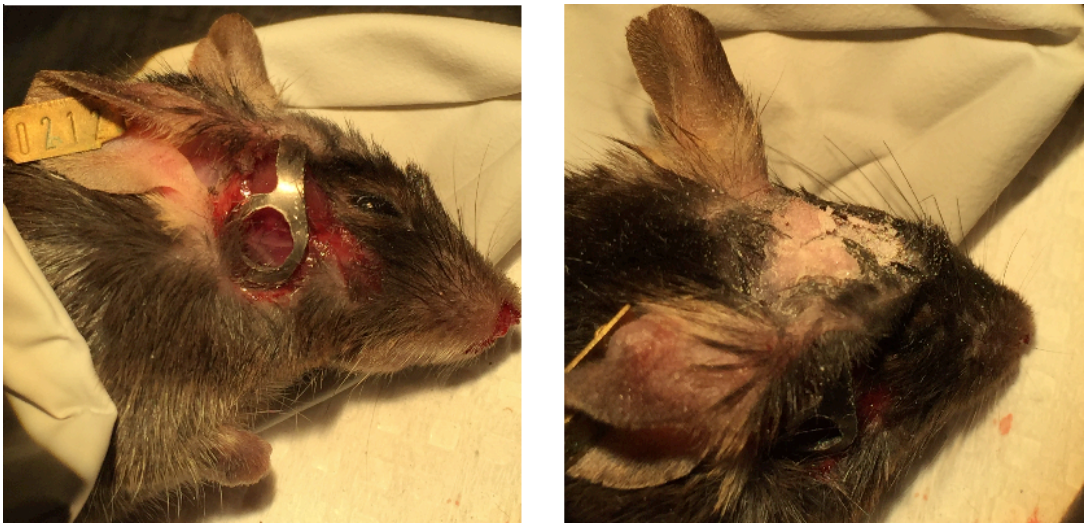

Figure 10. Nerve window positioning in mice (lateral and dorsal view). In the lateral view *(left)*, the pes anserinus, the buccal and marginal mandibular branches of the facial nerve are visible through the window. Skin was not glued onto the coverslip underneath the window in this image. In the dorsal view *(right)*, the dental resin creates a layer suitable for skin to adhere to.

Isoflurane is then switched off and the mouse is maintained on 1 L/min O_2 by nose mask until return of toe pinch response. Antibiotic ointment is applied to all wounds and the mouse is then transferred to a clean, warmed cage and monitored until return of normal activity, such as whisking and self-cleaning, are observed. Meloxicam (1 mg/kg/day) is administered subcutaneously and buprenorphine (0.1 mg/kg/12h) as needed for 72 hours post-operatively. Animals were allowed 48h of recovery time after surgery before imaging. They are monitored for post-operative distress by trained technicians. To euthanize mice, 1.3-1.7 L/min of CO_2 is administered until cessation of breathing is observed for a

minimum of 2 minutes. Cervical dislocation is performed as a secondary means of euthanasia.

Clinical Appearance Scoring

Mice were assessed for post-operative behavior and potential discomfort using a previously described clinical appearance scoring system (te Velde et al., 2003). Categories of reactivity to animal handling, physical appearance, and behavior were scored by two individuals on a scale of 0 to 3 every other day until wound dehiscence around the window was observed in the mice. Reactivity to animal handling was assessed by gently tapping on the backs of the mice and determining the quickness of response. Physical appearance factored evidence of corneal abrasion, pica behavior, piloerection, hunched posture, and poor grooming. Behavior was assessed through witnessing whisking and self-cleaning behaviors. Weight of the mice was also documented and normalized relative to the weight on Day 1 post-implantation.

Tissue Processing for Histomorphometric Analysis

Post-explant buccal and marginal mandibular branches of facial nerve in mice, roughly 5 mm in length, were fixed in 2% phosphate-buffered paraformaldehyde (PFA) for 12 hours at 4°C. **Figure 11** depicts the precise location of the explanted nerve branches in rat models.

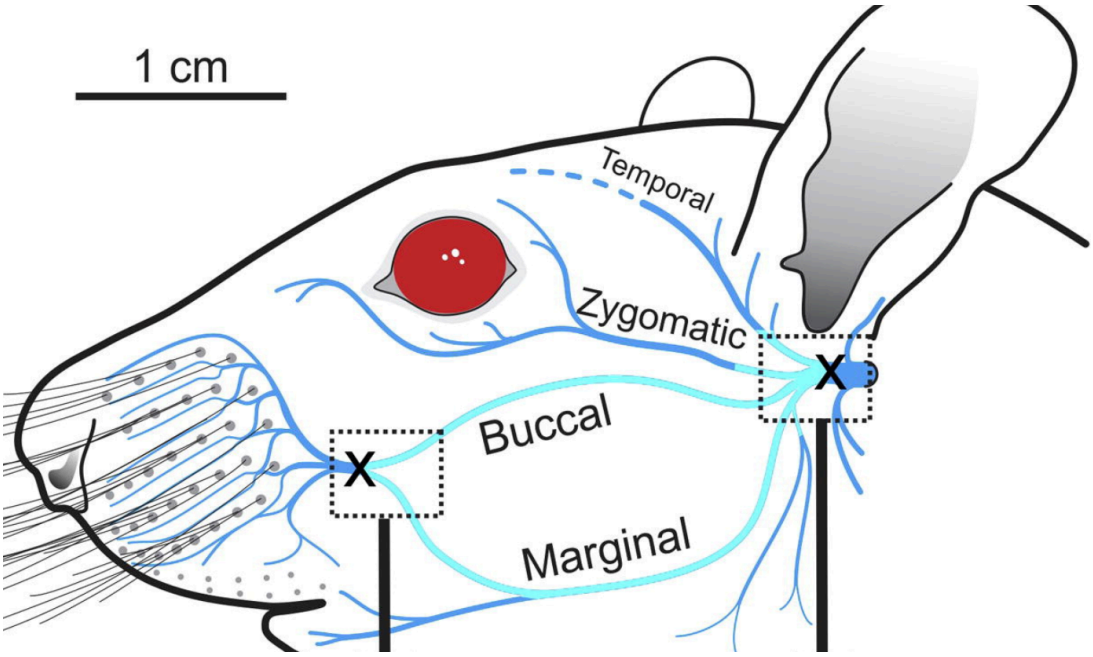

Figure 11. Diagram of the rat facial nerve depicting transection of the buccal and marginal mandibular branches of the facial nerve. Mouse facial nerve organization is similar to that in rats. Reprinted with permission from Heaton et al., 2014.

Nerves were rinsed thoroughly of PFA and placed briefly in 0.01 M phosphate-buffered saline (PBS). Samples were then dehydrated in 30% sucrose for 12 hours. Care was taken to ensure nerves were axially aligned on tongue depressors and not dislodged during the intermediary steps. Once dehydrated, the nerves were placed in a cryomold, flash frozen with liquid nitrogen and 2-methylbutane in optimal cutting temperature (OCT) compound (Tissue-Plus, Fisher Healthcare, Houston, TX). Each sample was sectioned using a cryostat (CM3050 S; Leica Biosystems, Buffalo Grove, IL) 1µm and 2µm thick on room temperature glass slides (Superfrost Plus, Fisher Scientific, Pittsburgh, PA). Sections were then stained with non-toxic fluorescent dye (FluoroMyelin® Red)

(1:300; Molecular Probes, Eugene, OR) or (FluoroMyelin® Green) (1:300; Molecular Probes, Eugene, OR) at room temperature for 20 minutes. They were then washed thrice with 0.01M PBS minutes 10 minutes at a time and mounted using medium that matched refractive index of the glass (Mount Liquid Antifade; Abberior GmbH, Göttingen, Germany).

Sections were imaged using a widefield fluorescent microscope (Axio Imager A.2; Carl Zeiss, Oberkochen, Germany), using a 20x objective lens (EC Plan-Neofluar; Carl Zeiss) and a light source (X-Cite 120 LED; Excelitas Technologies Corp., Waltham, MA). Samples were imaged using a 550/25-nm bandpass excitation filter, a 570-nm beam splitter, and a 605/70-nm emission filter, and acquired using a monochrome camera (Axiocam 503 mono; Carl Zeiss) with ZEN 2 Blue software (Carl Zeiss). Images were smoothed, cropped, and contrasted as necessary for enhanced visualization using ImageJ software (ImageJ, Fiji Distribution, Version 2) and axon counts were quantified by two individuals independently. Values are reported in terms of mean axon count with standard deviations. Myelinated axon number will be assessed for normality using the Shapiro-Wilk test. Groups are compared using the independent samples t-test with α set to 0.05.

Two-Photon Microscopy

Two-photon microscopy (2PM) was performed on a TrimScope platform (LaVision BioTec, Germany). 2PM excitation and SHG signal were obtained with a Ti:Sa tunable laser (InSight X3, Spectra-Physics) emitting in a range of 680nm

to 1300 nm. Images were acquired with a set of galvanometer mirrors (440 μm x 440 μm) and motorized LaVision BioTec xyz-stage. The laser beam is focused by a 20x, water immersion, NA 1.05 objective lens (Zeiss). Excitation and emission light are separated by a dichroic mirror (cut off at 720 nm), the emission light is split by dichroic mirrors (495nm long pass filter), auto-fluorescence and SHG signal is collected with two sets of filters (Semrock 461/10 nm and 525/50 nm) and detected by two LaVision BioTec GaAs High Sensitivity photomultiplier tubes (PMT).

Stimulated Raman Spectroscopy

Imaging was performed in vivo on an Olympus BX61WI upright microscope with FV300 scanning unit. The laser source employed was Emerald Engine from A.P.E. with a frequency doubling unit, resulting in two spatially overlapped beams of 2-ps lasers. The Stokes laser had a wavelength of 1031 nm and applied a power of 71 mW to the sample. The laser source had a tunable output (Levante IR ps, A.P.E., Germany) for pump beam and had a wavelength of 797 nm with an applied power of 185 mW to the sample. The energy difference of the photons from the two wavelengths was around 2,850 cm^{-1} to target the CH_2 stretching vibration in lipids. The 1031 nm laser was modulated by an electro-optical modulator at 10 MHz and transmitted to a scanning microscope. Lasers were focused on the sample using either a 40X, water-immersion, NA 0.8 objective lens (Zeiss) or a 60X, water-immersion NA 1.2

objective lens (Olympus UPLANAPO). Z-stacks of images were taken up to a maximum depth of around 60μm at a step size of 0.5 μm. Light through the sample was collected by a Nikon oil-immersion NA 1.4 condenser and filtered by a band-pass filter (Chroma, coherent anti-Stokes Raman scattering 890/220). The 797 nm pump laser was illuminated on a silicon photodiode detector (OSI Optoelectronics, S-100CL). The photocurrent was amplified by a filtered transimpedance amplifier and demodulated by a lock-in amplifier. The signal was then sent for data acquisition and the tissue image was able to be resolved on a personal computer.

RESULTS

Development of Facial Nerve Window Design

Several iterations of the nerve window were created and evaluated before the design was finalized. 3D models are shown in **Figure 12**. Need specifications were as follows:

(1) a method that permits adequate field-of-view of at least 4mm and resolution under high numerical aperture microscope objectives of at least one of the main branches of the facial nerve (buccal and marginal mandibular)

(2) a method that minimizes respiratory- and cardiac-induced motion artifact from the anatomical position of interest as well as ensures precise XYZ-coordinate positioning parallel to objective lens.

(3) a method that can be tolerated in murine models for resuming daily vital functions post-operation.

(4) a method with an associated protocol that is capable of being reproduced efficiently and consistently by scientists unfamiliar with mouse surgery and nerve microsurgery.

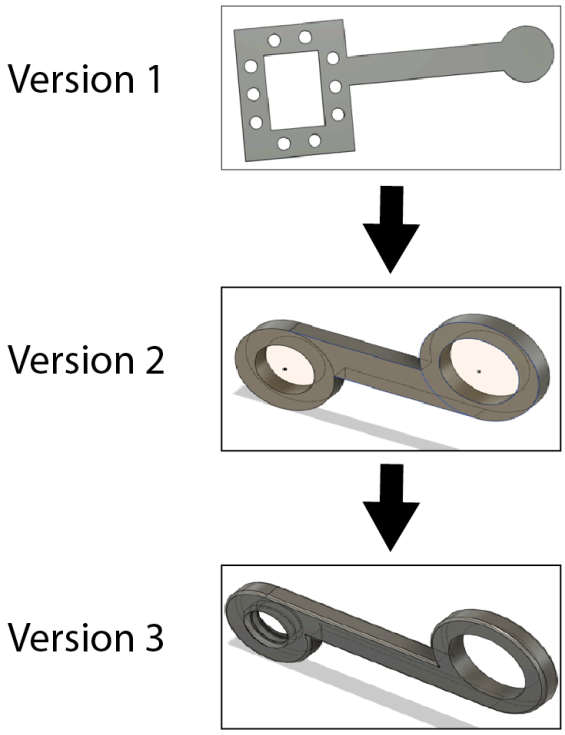

Figure 12. Design history of nerve windows. Version 3 is the current iteration. Key differences include the rectangular frame and suturing holes in Version 1, the two through-holes and shorter bridging piece in Version 2, and a M2.5 tapped-hole and through-hole connected by a longer bridging piece in Version 3. Dimensions are not provided for Version 1 and Version 2. Dimensions for Version 3 are found in Figure 5 of *Methods.*

The first iteration consists of a low-weight, titanium-built rectangular frame with through-holes meant for suturing the frame onto the skin. A bridge connects the rectangular frame to a circular head mount. Advantages to this design include the use of titanium alloy, which is light, corrosion resistant, biocompatible, and does not induce inflammation post-implantation (Niinomi et al., 2003). Furthermore, using the calvarium as a method of fixation has been well-documented in aforementioned cranial window protocols. Disadvantages to this

design include: (i) the complexity of suturing which limits performing such a procedure to skilled researchers, (ii) the likelihood of mice to bite or pull at the sutures leading to a potential source of infection prior to them dissolving, (iii) commercial unavailability of rectangular cover slips that matched the dimensions of the design, (iv) cost of titanium parts relative to other stainless biocompatible alloys capable of achieving similar outcomes, and (v) lack of a method to minimize motion artifact with this design.

The second iteration describes a low-weight “bridging piece” connecting two through-holes built from titanium, capable of being bent to reflect the geometry of facial skeleton. Circular holes for viewing were adopted rather than a rectangular window based on the relative commercial availability of 5mm and 8mm diameter circular coverslips. A rim with enough thickness between the inner and outer diameters of the through-holes was created for skin to be surgically glued onto the window fixture itself. While this method optimized fixation onto the periosteum and was shown to be well-tolerated (see *Qualitative Observation Studies in Nerve-Window Implanted Mice)*, we had challenges with minimizing motion artifact due to lack of external fixation when using two-photon microscopy. Results are indicated in *Two-Photon Microscopy* and the implications of this are discussed in greater detail in *Discussion*.

The third and final iteration is similar in shape to the second iteration, but has one tapped-hole and one through-hole 4mm in inner diameter and is built out of Stainless Steel 316 (SS316) rather than titanium. While titanium has greater

strength and lower weight, it is significantly more expensive than SS316. For the purposes of the study described and its use for imaging facial nerve regeneration, the use of SS316 was justified as it did not significantly increase weight beyond what the mouse was capable of tolerating, it was capable of lasting without any complications for the typical time-course of chronic imaging, and it was economical for high-volume mouse studies. The tapped-hole was added to incorporate the additional external fixation mount for the goniometer as seen in Figure 6 of the Methods for ensuring consistency of head placement. With this design, all need specifications were met. Surgical protocol was optimized as needed with this finalized nerve window design.

Qualitative Observation Studies in Nerve Window-Implanted Mice

In the first qualitative study using Version 2 of the nerve window, the goals were to:

(1) confirm whether our initial surgical procedure was a valid method of implanting the FNW.

(2) determine how long mice could tolerate the implanted windows without any adverse effects to health.

(3) characterize behavioral responses with implanted FNWs.

(4) characterize the integrity of FNW with regards to skin-metal interface, wound dehiscence, coverslip integrity, fluid buildup, and drift from anatomical position of interest.

Two male B6.Cg-Tg(Thy1-YFP)16Jrs/J mice underwent surgical implantation and were imaged using an operating microscope up on Days 3, 6, 8, 10, and 13 before signs of animal injury were observed on Day 13. Images taken from the 13-day study are shown and described in **Figure 13**. Post-implantation and removed from anesthesia, mice regained whisking function within 15 minutes, indicating no functional damage to facial nerve. Some initial unsteady gait was observed for 30 minutes as mice recovered. They resumed normal self-cleaning behavior and were able to eat and drink normally. For 48 hours, mice were administered meloxicam and buprenorphine per protocol and allowed to recover before imaging. Mice did not show any pica behavior, hyperpnea, piloerection or hunched posture, all typical signs of pain post-procedure. On Day 13 of imaging, the coverslip had detached from the nerve window in one mouse making visualization difficult without fluorescence. The nerve window fixture also showed significant drift from its initial position, signaling that the window had detached from the cranium. Skin had also detached from the nerve window. In the second mouse, the skin lost adherence to the window as well creating an open wound in the mouse. While visibility could be regained from re-attachment, the study ended and the mice were promptly and humanely euthanized per protocol to minimize suffering.

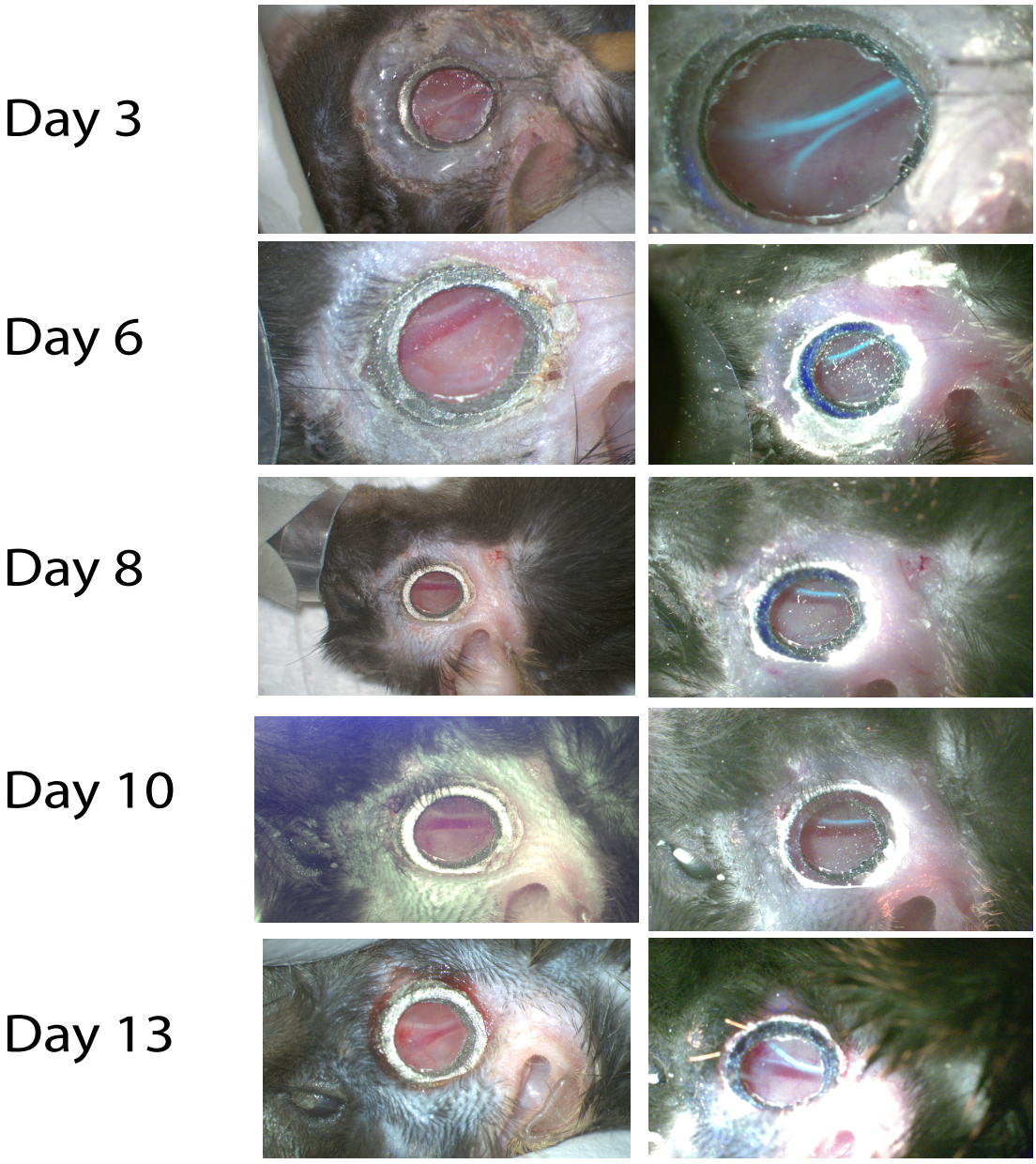

Figure 13. Characterizing response from implanted nerve window for 13 days in a Thy1-YFP mouse. Images were taken using a standard operating microscope. Pictures in the right column were taken under fluorescence filter. As displayed here, the buccal branch of the facial nerve was visible on all days of imaging. On Day 10, adherence of capillaries onto glass coverslip were visible. On Day 13, dehiscence of the window from the skin is visible. Images on Day 13 were taken by reorienting the window in place manually.

In the second qualitative study, modifications were made to the FNW and associated surgical protocol. Goals of this study were to characterize:

(1) any unusual behavioral patterns using Version 3 of the FNW

(2) compare any differences between titanium versus SS316 windows

(3) determine how low long mice could tolerate the implanted windows after changes to protocol

One Thy1-YFP mouse underwent surgical implantation and was imaged every week under operating microscope for 28 days (data not shown). Just like the mice in the first qualitative study, the mouse regained whisking function, vital functions, and normal apparent behavior shortly after the procedure. The results indicate that there were no apparent differences between titanium versus SS316 windows in terms of qualitative functional outcomes. Visibility through the window was consistent with the results from the first study. On Day 26, the mouse started observing hunchback posture as the nerve window lost some adherence to the skin. On Day 28, the window had completely detached from the skin. The mouse was promptly euthanized and the second qualitative study was discontinued.

Clinical Appearance Scoring

Thy1-YFP (N = 4, 44 days old) were implanted with FNWs and were scored by two individuals on Days 2, 3, 7 and 8 over a 9-day interval for reactivity to animal handling, behavior, physical appearance, and weight. For the four procedures, mean procedure time was 54.5 mins ± 20.4 mins including time of

induction, analgesia, hydration, shaving, surgery, and ointment application. Mean surgical time was 28.3 mins ± 6.7 mins from incision to closure. One mouse displayed signs of corneal abrasion post-implantation, displayed hunching posture, expressed delayed reactivity when provoked, and was humanely euthanized on Day 2. A majority of normal scores were found across all four timepoints for each mouse. Post-implantation, slight weight loss was observed (~7% of total body weight) by Day 2 in 3 animals but one. All mice weights were within normal limits with respect to their age in weeks as per a reference C657BL/6J growth chart provided by Charles River Laboratories, Inc. (Wilmington, MA). A steady increase in weight was observed afterwards in the three remaining mice. Mice did not show signs of immobility, signs of concerning behavior, and displayed standard grooming behaviors. Whisking function was videotaped by gently holding onto the nerve window threaded rod affixed onto its head. During this step, one mouse had its window pulled out, exposing the wound site and had to be humanely euthanized on Day 7. Occasional scratching behavior was observed surrounding the window for the first 4 days post-implantation. Signs of inflammation and wound dehiscence were not present until Day 9 in the two remaining mice. Results are summarized below in **Figure 14** and **Figure 15.**

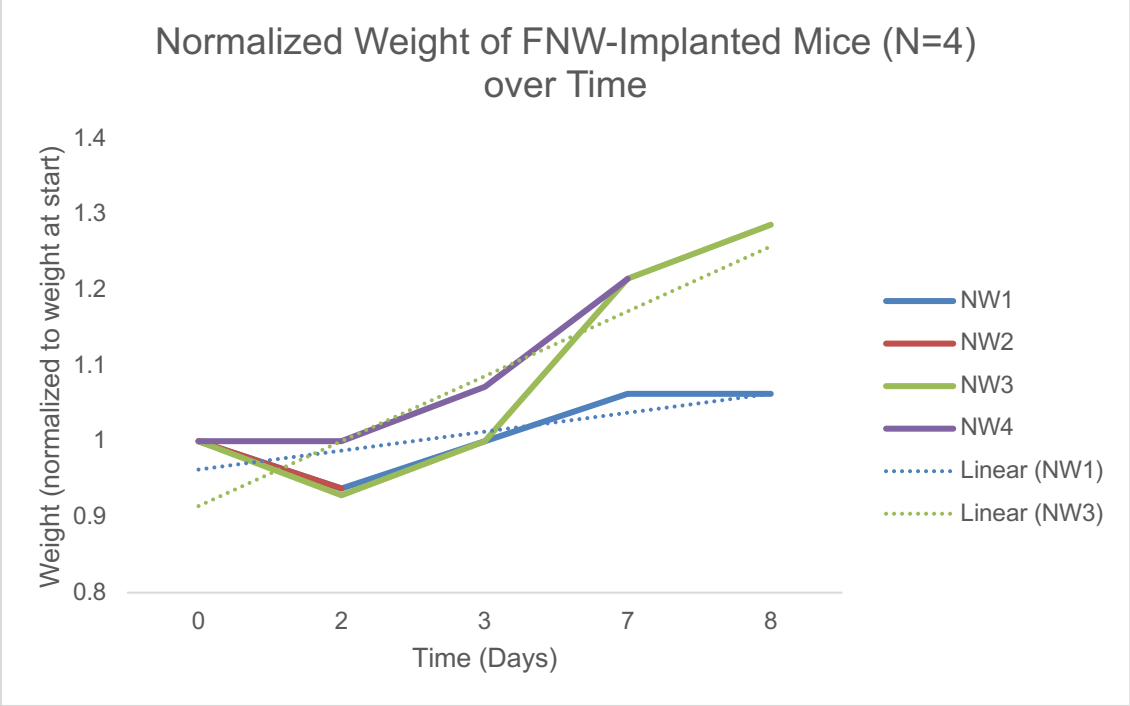

Figure 14. Normalized Weight of FNW-implanted mice over time. Weight of the 4 FNW-implanted mice, named NW1 to NW4 in order of time of implantation, was measured five times over 8 days and plotted over time. Values are normalized to the weight of the mice on Day 1 after surgical implantation. NW2 displayed signs of poor tolerance to the window and was euthanized on Day 2. NW4 had a dislodgment of the window upon manual manipulation and was euthanized on Day 7. Linear trendlines for NW1 and NW3 are shown and demonstrate a general positive increase in weight.

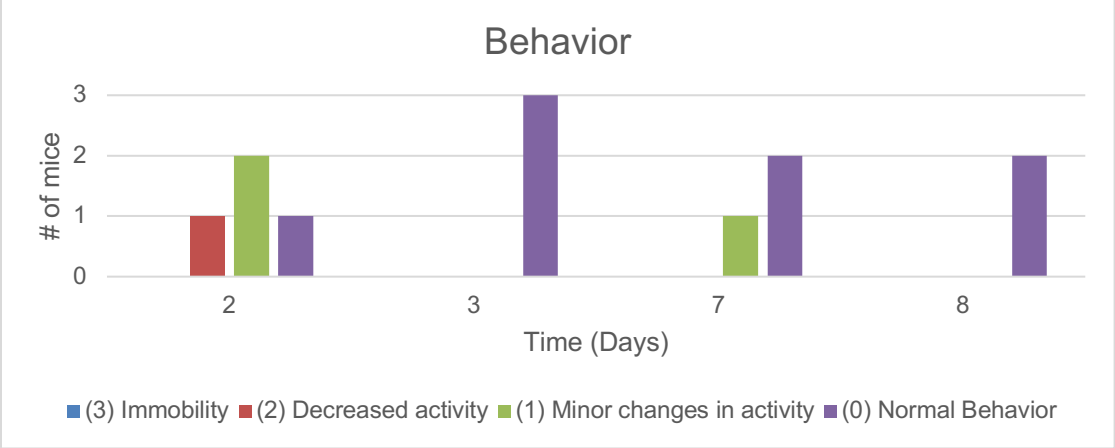

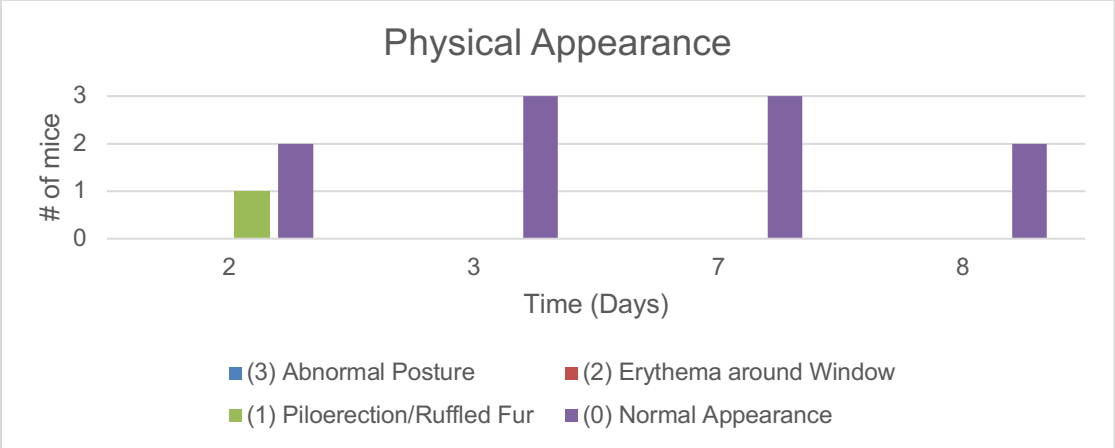

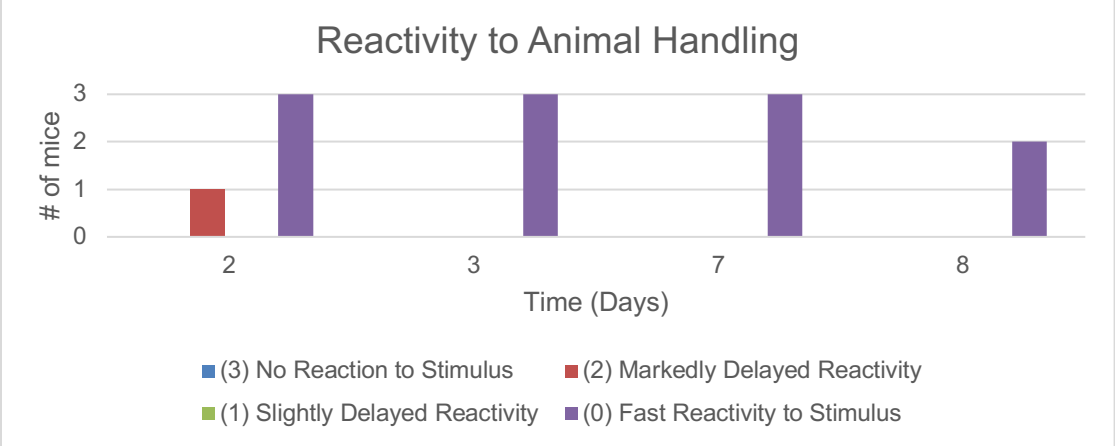

Figure 15. Number of FNW-implanted mice expressing changes in behavior, appearance, and reactivity at four separate timepoints. Mice (N=4) were scored by two observers on a scale from 0 to 3 where 0 represents normal behavior and 3 represents severe clinical concern.

One mouse was euthanized on Day 2 after scoring. Another mouse was euthanized on Day 7 after scoring.

Nerve Histomorphometry and Myelinated Axon Counting

Myelinated axon counts in healthy and FNW-implanted mice (ages ranging from 25 days old to 84 days old) were quantified to assess any window-induced neuropathy from longitudinal compression onto the nerve. Buccal (N=7) and marginal (N=6) branches of the facial nerve from healthy C57 and YFP mice were employed and processed for cryosectioning and imaging as discussed above. Mean myelinated axon counts and standard deviations for both branches was determined through manual counting from digitized images by two independent observers in ImageJ software (ImageJ, Fiji Distribution, Version 2). Power analysis was performed to determine the suitable number of samples necessary to detect an effect of potential FNW-induced neuropathy. The mean number of myelinated axons in buccal branches of healthy mice was 947.6 ± 129.9 and the mean number of myelinated axons in marginal mandibular branches of healthy mice was 801.3 ± 145.1. Data exhibited normality using the Shapiro-Wilk test. With α of 0.05 and a power of 80% (two-tailed), it would require N=7 buccal branches and N=12 marginal branches to detect a 15% difference in myelinated axonal counts between groups of control versus FNW-implanted mice.

In Thy1-YFP mice, FNWs were implanted unilaterally and later removed after 9 days (N=3). Due to protocol limitations and delays in manufacturing, only 3 mice (those from *Clinical Appearance Scoring Study*) were used. Buccal (N=3) and marginal mandibular branches (N=3) of the facial nerve were harvested bilaterally (from healthy side of the face and the window side of the face) and steps were repeated as above. A cross-section of a marginal mandibular nerve is displayed in **Figure 16**. The mean number of myelinated axons in buccal branches of FNW-implanted mice was 799.3 ± 128.6 and the mean number of myelinated axons in marginal mandibular branches was 738.0 ± 197.2. Assumptions of normality and equal variances were determined to be valid in both healthy and FNW-implanted groups for buccal and marginal mandibular counts. Comparing the numbers, there was no significant difference in myelinated axon counts in buccal branches in healthy versus FNW-implanted mice, $t(8) = 1.7$, $p = .136$. There was no significant difference in myelinated axon counts in marginal mandibular branches in healthy versus FNW-implanted mice, $t(7) = 0.55$, $p = .599$.

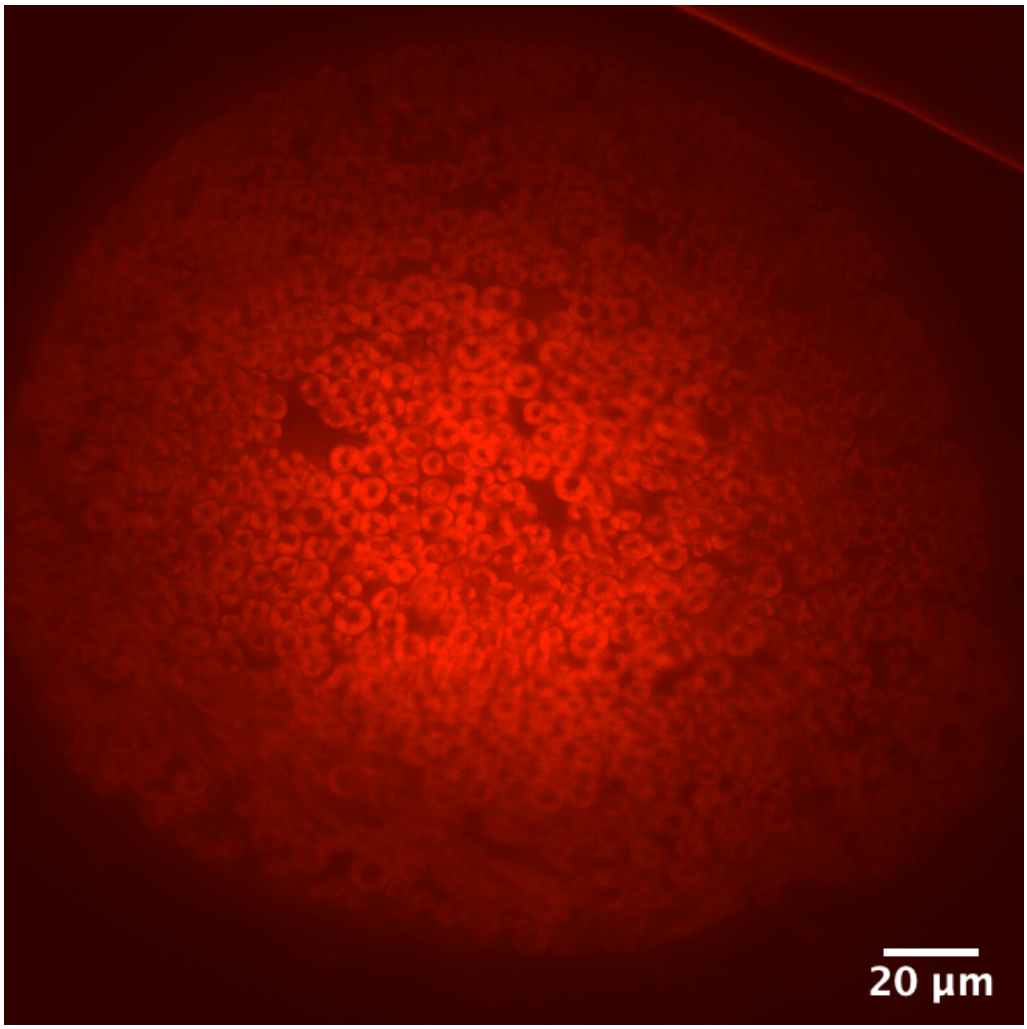

Figure 16. FluoroMyelin® Red-stained cross-section of murine marginal branch after window implantation. Displayed is an optimal cutting temperature compound-embedded, 1-µm sectioned, FluoroMyelin® Red-stained cross-section displaying stained rings of myelinated axons. Image was captured using widefield fluorescent microscopy and processed for contrast, brightness, sizing and color using ImageJ. Scale bar 20 µm.

SRS Imaging of Facial Nerve Environment

One healthy C57BL/6J and one 48h post-Sunderland Type V injury mouse were implanted with FNWs and euthanized as per the protocol in *Methods*. Within 1.5h of euthanasia, SRS imaging was performed through the windows and allowed for label-free resolution of myelin sheaths of the buccal branch of the facial nerve. Intrinsic contrast allowed for myelin tubules to be visualized relative to the interspersed dark background up to around 30μm until significant attenuation was observed. **Figure 17** shows the comparison between longitudinal and transverse sections of normal and injured murine facial nerve. In the normal longitudinal section, resolution allowed for identification of nodes of Ranvier spaced between axons. In the 48-hours post-injury longitudinal section, neural demyelination and discontinuity are evident in certain axons with the lack of coherent scattering signal observed, ovoid bodies and hollowed-out patterning, and increase in debris among axons that have yet to undergo degeneration. This is consistent with the previously described stages of Wallerian degeneration where myelin sheath organization begins to disintegrate distal to where the injury occurred (Fu & Gordon, 1997). Samples were then harvested *ex vivo* and sectioned for imaging.

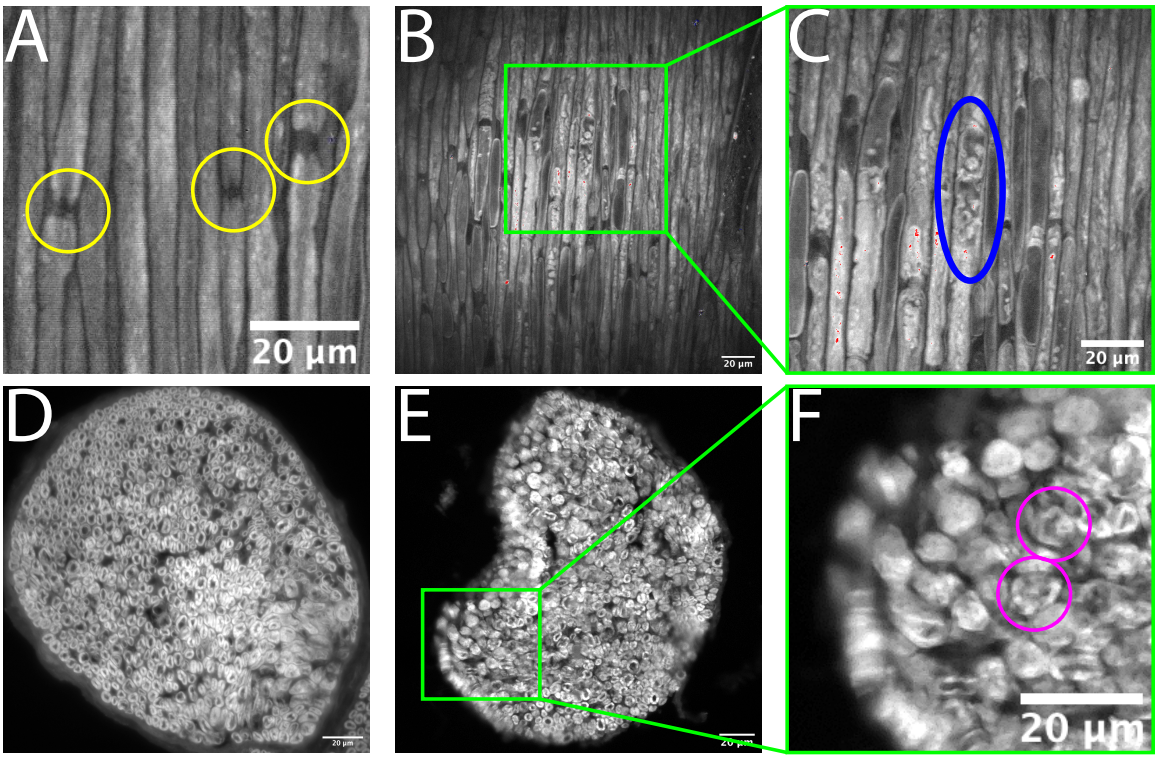

Figure 17. Longitudinal and cross-sectional images of buccal branches of murine facial nerve from healthy C57BL/6J and injured C57BL/6J mice. (A) Stain-free SRS image of myelin in a longitudinal buccal branch nerve segment in healthy C57BL/6J mouse (30 µm depth). Nodes of Ranvier are clearly visualized between axons (yellow circles). **(B)** Stain-free SRS image of myelin in a longitudinal buccal branch nerve segment in C57 mouse 48h post-injury (30 µm depth). **(C)** Evidence of ovoid bodies signaling demyelination typical of Wallerian degeneration (blue oval) is noted in injured mouse model. **(D)** FluoroMyelin® Red-stained transverse cross-section (1 µm) of myelin in buccal branch nerve segment in healthy C57 mouse. **(E)** FluoroMyelin® Red-stained transverse cross-section (1 µm) of myelin in buccal branch nerve segment in C57 mouse 48h post-injury. **(F)** Magenta circles display poorly visualized myelin rings attributed to scattered myelin signal from axon discontinuity. Scale bars **(A-F)** are all 20 µm.

2PM Imaging of Facial Nerve Environment

Three separate imaging studies were performed with Thy1-YFP mice and are described below.

The first study was to demonstrate the use of 2PM to image the facial nerve environment in a live fluorescent reporter mouse model. Imaging was done through Version 2 of the nerve window. Mice were anesthetized using ketamine (75 mg/kg) and dexmedetomidine (0.25 mg/kg) administered intramuscularly. The glass coverslip was gently cleaned with isopropyl alcohol to remove external exudate. Then they were placed laterally over a hand-warmer under the microscope objective to maintain core temperature while under anesthesia. Effects of the anesthesia were reversed with atipamezole hydrochloride. In this session, there was no head fixture in place and no goniometer to ensure optimal angle of rotation. Because of motion artifact, the maximum-intensity projection shown did not allow for resolution of individual axons and is therefore not shown. Furthermore, head tilt occurred as the objective moved axially downwards, shifting the focal plane of imaging. To demonstrate the isolated effect of respiratory- and cardiac-induced motion artifact, single images were collected at frequencies of 400, 600, 800, and 1000 Hz and are shown side-by-side in **Figure 18**. Laser power was exponentially corrected for depth to achieve an adequate signal-to-noise ratio at deeper layers of the nerve. Image data was imported into ImageJ (ImageJ, Fiji Distribution, Version 2) for visualization and adjusted to optimize contrast.

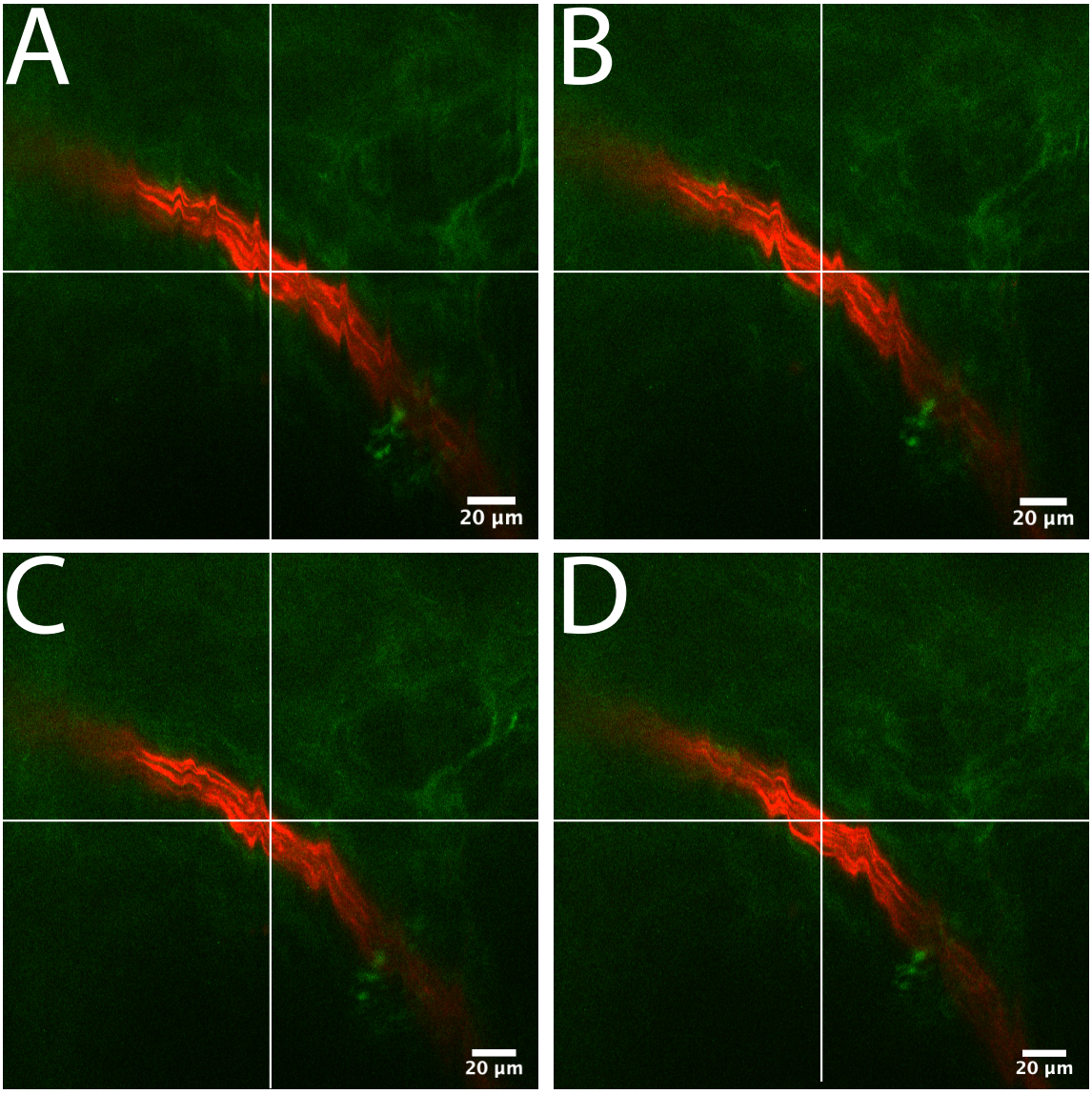

Figure 18. 2-channel intravital imaging of the buccal branch of murine facial nerve using 2PM taken at (A) 400 Hz, (B) 600 Hz, (C) 800 Hz, (D) 1000 Hz. 3-line averaged images were taken at same X-Y location and Z-depth. Movement artifact is demonstrated as the periodic wave-like shift of axons during image capture. YFP signal corresponding to axons is denoted as red and SHG emission corresponding to collagen is denoted as green. Scale bars **(A-D)** are all 20 µm.

The second study was to verify whether the microscope set-up matched the dimensions of the goniometer and the mouse head. A Thy1-YFP mouse was implanted with a FNW and a threaded rod and euthanized 48h post-implantation. Within 30 minutes of euthanasia, the animal was attached onto the goniometer fixture with its head positioned under the objective lens, rotated and tilted such that the imaging surface was parallel to the plane of the objective. After collecting X-Y images at increasing depths, a three-dimensional reconstruction of the axons and surrounding collagen matrix was developed using Imaris software (Bitplane Inc., Concord, MA) and is shown below in **Figure 19(A)** below. Depth was ultimately limited by the physical obstruction of the 1mm-thick metallic nerve window frame that circumscribed the objective lens.

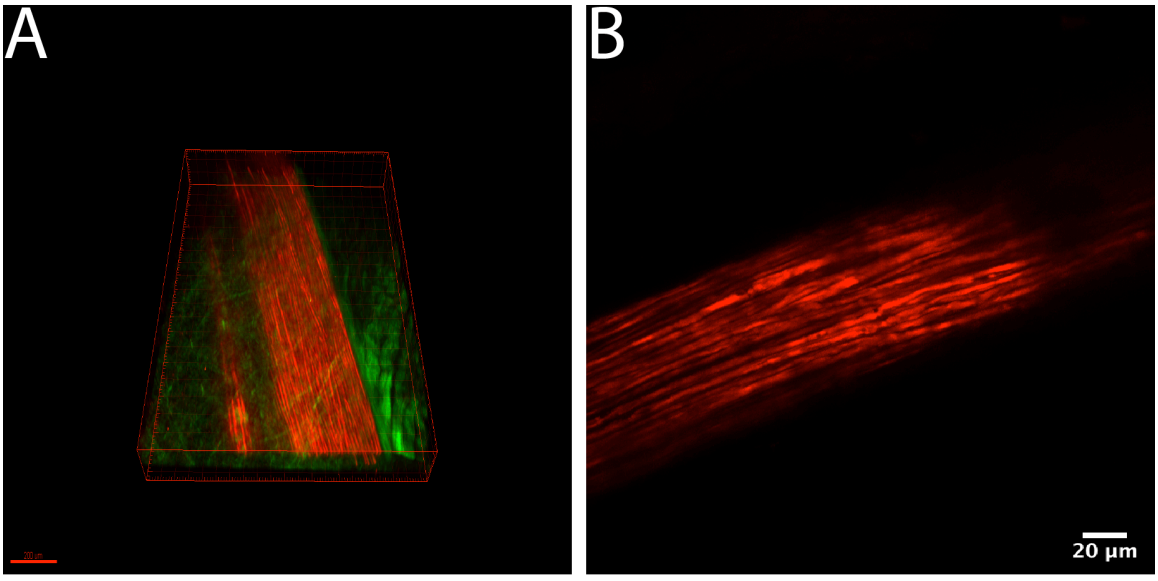

Figure 19. Intravital imaging of the buccal branch of murine facial nerve using 2PM with head fixation. (A) is a 2-channel, 3D-rendering of axon tracts (red - YFP) surrounded by collagen

matrix (green - SHG) taken in a freshly-killed Thy1-YFP mouse fixed onto a mount. Scale bar 200 μm. **(B)** is a 1-channel, maximum-intensity projection of axon tracts taken in a live Thy1-YFP mouse setting. Scale bar 20 μm.

The third study was performed with an optimized protocol stemming from the results of the first and second imaging sessions involving the use of an anesthetized live mouse fixed onto the goniometer-rail system. Similar issues regarding physical obstruction of the 1mm-thick metallic nerve window frame limited penetration depth of imaging. Results are shown in **Figure 19(B)** above.

DISCUSSION

Summary

Pioneering bright-field IVM techniques allowed for landmark investigations into biological phenomena such as Antony van Leeuwenhoek's work describing how blood circulates through vessels or Henri Dutrochet's research into how leukocytes extravasate into inflamed tissues (Dutrochet & Glasgow, 1824; Leeuwenhoek & Hoole, 1800). IVM has made remarkable transformations centuries later and now allows us to revisit and re-address such biological paradigms to refine understanding of mechanisms. At present, however, there is a need for methods to achieve high-resolution imaging at depths greater than 100 μm to characterize phenomena that occur over longer periods of weeks to months in complex tissues. Imaging techniques that rely on repeat surgical dissections to expose the imaging site can result in tissue dehydration, impaired thermoregulatory control, risk of infection or adverse effects of chronic anesthesia exposure (Kedrin et al., 2008). In the study of peripheral nerve regeneration, repeat surgical manipulation carries risk of nerve insult, which may confound analysis of the biological microenvironment of interest (Jung et al., 2014). Furthermore, performing multiple surgeries in individual animals to achieve sufficient statistical power may introduce considerable variability that limits interpretation of experimental outcomes.

Herein, we report initial serial characterization of the facial nerve microenvironment using a facial nerve window comprising of a stainless-steel

implant with an affixed 8mm coverslip anchored to the cranium. A head-post is inserted allowing for the mouse to be fixed externally to a dual-axis goniometer allowing for fine rotational control of the neck and an imaging plane parallel to the objective lens. Through this window, we report efficacy of our proposed model by reliably obtaining high-resolution images of the facial nerve axons and surrounding collagen matrix through the window in adult fluorescent Thy1-YFP mice using 2PM imaging. We are able to claim through a qualitative 13-day study the ability to serially image the facial nerve microenvironment without opacification over a timescale pertinent to murine facial nerve regeneration. Furthermore, we were able to demonstrate clinical safety of the FNW through a previously documented clinical assessment scoring protocol and subsequent histomorphometric analysis of myelinated axon counts in healthy and implanted mice. Finally, we demonstrated the ability to resolve differences in axon myelination among peripheral nerves from healthy and injured wild-type mice using label-free SRS microscopy.

Surgical Procedure Considerations and Limitations

The efficacy of our proposed facial nerve window technique for serial intravital high-resolution imaging of the murine facial nerve was demonstrated through good post-surgical recovery and behavior tracking, preserved clarity of the imaging window over a two week period, and absent significant changes in nerve histomorphometry between implanted animals and healthy controls.

The current specifications of the facial nerve window described herein allows for a stable, appropriate field-of-view of at least two critical branches of the facial nerve. The implant frame, developed using stainless steel 316 alloy, is biocompatible and demonstrates excellent strength-to-weight ratio. Other benefits of the model demonstrated over the course of this study, include the ability to directly access the coverslip for cleaning external exudate using alcohol wipes and the reproducible and efficient protocol that takes less than thirty minutes to perform by lab personnel initially unfamiliar with surgical techniques. With practice, we predict operating time will further decrease, and the success rate of implantation will increase beyond what was achieved in this preliminary study.

Limitations to the model include: (1) the inability to clean exudate from the deep aspect of the glass coverslip window, (2) the occasional detachment of the skull bone-to-implant anchoring upon manual manipulation, (3) incomplete evaluation of morphological, cellular, and biochemical changes that may occur (inflammation or perfusion) before 10 days at the local and systemic level, and (4) incomplete assessment of quantifiable functional outcome such as an electrophysiological arm or walking track analysis typically present in contemporary studies like ours. We intend on performing testing of (3) and (4) in the near future. Regarding (1), we found over the course of the study some difficulty in ensuring hair was meticulously shaved and removed around the operating site. Tissue exudate or external hairs can disrupt optical clarity and

image quality necessitating a solution for more optimal microscopy. Future studies will evaluate the use of hair removal creams prior to procedure. We will also reconsider design requirements especially when using water-immersion objectives that may result in leakage of water under the coverslip if it is not properly glued onto the frame. Of the two failures in surgical outcomes in mice employed for our study, both were due to issues with (2). In particular, we found the use of Ortho-Jet, a dental resin indicated for use in orthodontal procedures, to be the critical and most challenging (>15 minutes) step in the procedure. In one mouse, the direct application of the powder onto the cranium resulted in corneal abrasion that went unnoticed during operation. In another, edema from the vessels within the galea aponeurotica resulted in the apparent inability to create a dry enough periosteum for the anchoring and cementation of the implant. Over several days this went unnoticed until a rapid jerk during manual manipulation caused detachment and rendered the mouse susceptible to infection requiring that it be euthanized humanely. Of note, because there is an absence of edematous leakage in freshly-killed mice, we found it significantly easier to secure the implant and demonstrate peripheral nerve imaging, as we did in the SRS imaging arm of the study. Future studies will go towards using cements that have been documented with more reported success. If powders are necessary for use, we intend to use a more rigorous surgical draping prior to procedure to protect from future corneal abrasions or skin irritation.

Histomorphometric Analysis Considerations and Limitations

An assumption was made *a priori* to our study that myelinated axons represent the majority of axons in the facial nerve buccal and marginal mandibular branches. This assumption was based upon a study by Shimozawa in 1976 that the facial nerve in mice distal to the geniculate ganglion consists of, on average, 93% of total nerve fibers being myelinated and only 6.3% unmyelinated (Shimozawa, 1976). Furthermore, because buccal and marginal mandibular branches provide motor function to facial musculature, and, for motor neurons to generate rapid action potentials, they require myelination, we believe our assumption is valid. Because demyelination is a distinct observable step in nerve injury, we sought to demonstrate that no induced neuropathy occurred as a result of the window through quantification of myelinated axon counts, which is presently the most used parameter to measure peripheral nerve regeneration (Wood et al., 2011). We report no significant difference in myelinated axon counts for both buccal and marginal mandibular branches in control C57 mice versus FNW-implanted Thy1-YFP mice, implying no apparent effect of the window. The average caliber of marginal mandibular nerve branches was measured to be about 182.38 μm ± 15.35 μm in diameter while that of buccal nerve branches was shown to be about 187.19 μm ± 42.96 μm in diameter. Of note, the founder mice for Thy1-YFP mice were wildtype C57BL/6J mice, allowing for us to assume genomic equivalence and readily compare axon counts from both mice despite the YFP gene insertion. To our knowledge, we are

unaware of any study that has been able to successfully prepare and quantify axon count from specimens expressing fluorescent protein due to leakage from cells when membrane integrity is compromised during the freezing and sectioning steps. Therefore, we employed the use of FluoroMyelin® as an exogenous stain for myelin.

The major limitation to the histomorphometric analysis described herein is that we were unable to perform our study at 80% power to detect a 15% difference in axon counts. The required numbers were N=7 and N=12 for buccal and marginal mandibular branches in FNW-implanted mice respectively whereas the actual numbers reported in our study were N=3 and N=3 respectively. This was due to external time and resource constraints of the study. Therefore, it is likely that an underpowered study may have resulted in a greater likelihood of type II error and effects of practical importance may have gone undetected. Despite this, we believe the results of the clinical assessment scoring, which were a majority of normal scores at all time-points for the 3 implanted animals (not including the one from Day 2), indicate that any nerve damage that may have occurred was of clinical insignificance. For the purposes of our study however, it is crucial for the window to demonstrate no adverse effects to the microenvironment for proper visualization and characterization. We therefore see achieving appropriate statistical power as a major priority in future work.

Another limitation to the analysis is the reliance on manual counting which can result in reported measurement inaccuracies. For this reason, two raters

were employed in addition to the first author in counting myelinated axons and subsequently averaged. Raters were provided a random assortment of images from both testing groups in a blinded fashion. Future work will go towards leveraging artificial intelligence-based softwares that can process raw images and segment them for analysis.

Intravital Imaging Considerations and Limitations

Direct imaging of nerves provides comprehensive information about the nerve microenvironment unlike any methodologies that quantify functional outcomes such as histomorphometry, electrophysiology, or behavioral video tracking. The use of advanced optical microscopy through exogenous stains or genetic labels as well as microscopic techniques such as multiphoton excitation and stimulated Raman scattering can provide robust structural information about peripheral nerves that the aforementioned methods cannot, for example. Therefore, we demonstrate the use of our FNW in imaging various cellular structures within the neural microenvironment using two-photon microscopy with fluorescent reporter mice and using SRS with wild-type mice.

Using two-photon microscopy, we were able to visualize axon tracts longitudinally and the surrounding collagenous matrix of the neural epineurium and perineurium. Mice were able to tolerate the ketamine/dexmedetomidine anesthesia and recover within 30 minutes of imaging without any visible complications. However, imaging depth proved to be the major limiting factor in

the 2PM studies due to the physical obstruction of the objective lens contacting the outer metal rim of the implant (1mm thick in the z-direction). This resulted in an ability to collect images at a maximum of 75μm in depth from the surface of the nerve. Future work will go towards redesigning the thickness of the implant for increased depths of imaging as well as attempting techniques such as tissue clearing. This will allow us to limit the effects of light scattering through turbid tissues from the various layers that alter focal spot geometries by infusing chemicals that homogenize index of refraction. Jung et al. documents the benefits of such a technique in acquiring a volumetric profile of the axons within a nerve fiber, analyzing myelination patterns of healthy versus degenerating axons, and describing the results in the context of what is already understood about Wallerian degeneration and regeneration (Jung et al., 2014).

In this study, we also demonstrate through proof-of-concept that SRS imaging of normal and injured facial nerves is achievable through FNWs in mice. Although mice were imaged at just one time-point, we are able to show that nerve demyelination through loss of myelin sheath organization was observed 48h post-injury which is consistent with previously documented patterns of nerve degeneration in mice. Because demyelination and remyelination steps in nerve occurs over a time-frame of several days to weeks, the benefit of a chronic imaging window is evident in being able to monitor the same field-of-view to micrometer precision serially.

Movement artifact is one of the major challenges that impedes intravital peripheral nerve imaging. To address this, some studies report the use of external fixation onto an imaging stage to minimize this (Meijer et al., 2017). Results from our 2PM first and third studies (**Figures 18 and 19(B)**) show the difference in image quality when efforts are taken such as external head fixation to limit respiratory- and cardiac-induced movement artifact. Some studies have addressed this issue using custom, real-time correction algorithms to correct images for animal movement where fixation is not possible (Henry et al., 2009; Lorenz et al., 2012; Ritsma et al., 2013). Other studies obtain images at a video-rate that coordinates image capture with respiration when possible (Dunn et al., 2002). Between murine models too, rats demonstrate a larger degree of movement artifact compared to mice in part due to its larger size, which can be an important reason for choosing the latter for imaging studies instead (Grochmal et al., 2018).

The main limitation to our SRS proof-of-concept demonstration is that it was not performed in living mouse models, which limits what we can claim about our proposed model for serial imaging. Although the mice were freshly-killed and imaged within 1.5-2 hours, it is possible that axonal degradation due to cell death may have played a confounding factor in assessment of nerve injury. However, images of the healthy mouse do not show signs of any degeneration and are markedly different from those of the injured mouse as explained in *Results.* Another limitation with the proposed SRS study lies in the limited imaging

penetration of 30μm that was possible before signal to noise ratio deterioration occurred. At present, there is limited reporting of penetration depth achieved using Raman microscopy techniques. However, of those that have reported such information, our reported imaging depth falls within a general range of 20 μm – 100 μm (Drutis et al., 2014; Evans et al., 2005; Hill et al., 2020; Wang et al., 2007; Wei et al., 2019; Wright et al., 2007).

Future experimentation is underway to determine whether healthy and injured mice can be imaged under SRS through its nerve window at several time-points over the course of nerve demyelination and remyelination. Evidence of a serial study using SRS without the use of a chronic imaging window has been documented previously for the sciatic nerve setting (Henry et al., 2009; Tian et al., 2016). Given our demonstrated results from 2PM using living mice, we believe that this limitation can be easily overcome with our current setup for the facial nerve.

Where identification of myelin sheath signal may be indicative of healthy or remyelinating axons or even recruitment of Schwann cells, the absence of such signal may indicate degenerating nerves. We believe SRS to have immense sensitivity therefore in assessing peripheral nerve injury versus available techniques although future studies will be necessary to quantifiably compare experimental outcomes. Clinical implications of a method that does not require exogenous labels, is highly lipid-sensitive, does not require high powered laser sources, and allows for in vivo imaging in a nondestructive manner are

numerous. One study demonstrated its use in revealing tumor margins in vivo during a live brain tumor surgery in mice (Ji et al., 2013). A proof-of-principle CARS endoscope was developed by Légaré et al. which may limit the invasiveness of surgical procedures involving nerve pathology (Légaré et al., 2006). In the peripheral nerve setting, specifically during nerve transfer procedures, success of reinnervation occurs when donor nerve axon load matches with a load that was previously inputted to the same muscle. Work in our lab is presently going towards comparing SRS methods for assessing onset of injury versus using rapid and automated histomorphometric axon counting as means of informing decision-making during cross-facial nerve grafting procedures. Though the clinical potential for SRS is clear, the most immediate utility of such a technique will ostensibly be in animal models. We claim therefore the novel use of an imaging chamber for successful visualization of facial nerve pathology using SRS techniques.

Conclusion

Herein, we describe the development and use of a peripheral nerve window for intravital imaging of the murine facial nerve microenvironment. The device was employed to obtain high-resolution three-dimensional images of the murine facial nerve under healthy and injury states using fluorescent and label-free imaging techniques. This approach enables serial imaging of nerve regeneration without the need for repeated surgical dissection, reducing animal harm and

experimental variability. The safety and efficacy of this approach was demonstrated through the use of clinical assessment scoring, functional observation and neural histomorphometric analysis. Future work will seek to employ this model in the study of mechanisms underlying neural response to injury and therapies to optimize nerve regeneration.

REFERENCES

Anzil, A. P., & Wernig, A. (1989). Muscle fibre loss and reinnervation after long-term denervation. *Journal of Neurocytology*, *18*(6), 833–845. https://doi.org/10.1007/bf01187235

Brendza, R. P., Bacskai, B. J., Cirrito, J. R., Simmons, K. A., Skoch, J. M., Klunk, W. E., Mathis, C. A., Bales, K. R., Paul, S. M., Hyman, B. T., & Holtzman, D. M. (2005). Anti-Aβ antibody treatment promotes the rapid recovery of amyloid-associated neuritic dystrophy in *PDAPP* transgenic mice. *The Journal of Clinical Investigation*, *115*(2), 428–433. https://doi.org/10.1172/JCI23269

Bridge, P. M., Ball, D. J., Mackinnon, S. E., Nakao, Y., Brandt, K., Hunter, D. A., & Hertl, C. (1994). Nerve crush injuries—A model for axonotmesis. *Experimental Neurology*, *127*(2), 284–290. https://doi.org/10.1006/exnr.1994.1104

Brodnick, S. K., Hayat, M. R., Kapur, S., Richner, T. J., Nonte, M. W., Eliceiri, K. W., Krugner-Higby, L., Williams, J. C., & Poore, S. O. (2014). A chronic window imaging device for the investigation of in vivo peripheral nerves. *2014 36th Annual International Conference of the IEEE Engineering in Medicine and Biology Society*, 1985–1988. https://doi.org/10.1109/EMBC.2014.6944003

Byrne, P. J., Stuart, R. M., Fakhry, C., Lehar, M., & Flint, P. W. (2005). An Electrophysiologic Model for Functional Assessment of Effects of Neurotrophic Factors on Facial Nerve Reinnervation. *Archives of Facial Plastic Surgery*, *7*(2), 114–118. https://doi.org/10.1001/archfaci.7.2.114

Carter, D. A., & Lisney, S. J. W. (1987). The numbers of unmyelinated and myelinated axons in normal and regenerated rat saphenous nerves. *Journal of the Neurological Sciences*, *80*(2), 163–171. https://doi.org/10.1016/0022-510X(87)90152-3

Chernousov, M. A., & Carey, D. J. (2000). Schwann cell extracellular matrix molecules and their receptors. *Histology and Histopathology*, *15*(2), 593–601. https://doi.org/10.14670/HH-15.593

Chudakov, D. M., Matz, M. V., Lukyanov, S., & Lukyanov, K. A. (2010). Fluorescent Proteins and Their Applications in Imaging Living Cells and Tissues. *Physiological Reviews*, *90*(3), 1103–1163. https://doi.org/10.1152/physrev.00038.2009

Dey, J., Ishii, M., Boahene, K., Byrne, P., & Ishii, L. (2014). Facial Reanimation Surgery Restores Affect Display. *Otology & Neurotology*, *35*(1), 182–187. https://doi.org/10.1097/MAO.0b013e3182a1ea8a

Dey, J. K., Ishii, M., Boahene, K. D. O., Byrne, P. J., & Ishii, L. E. (2014). Changing perception: Facial reanimation surgery improves attractiveness and decreases negative facial perception. *The Laryngoscope*, *124*(1), 84–90. https://doi.org/10.1002/lary.24262

Disegi, J. A., & Eschbach, L. (2000). Stainless steel in bone surgery. *Injury*, *31*, D2–D6. https://doi.org/10.1016/S0020-1383(00)80015-7

Drutis, D. M., Hancewicz, T. M., Pashkovski, E., Feng, L., Mihalov, D., Holtom, G. R., Ananthapadmanabhan, K. P., Xie, X. S., & Misra, M. (2014). Three-dimensional chemical imaging of skin using stimulated Raman scattering microscopy. *Journal of Biomedical Optics*, *19*(11), 111604. https://doi.org/10.1117/1.JBO.19.11.111604

Dunn, K., Sandoval, R., Kelly, K., Dagher, P., Tanner, G., Atkinson, S., Bacallao, R., & Molitoris, B. (2002). Functional studies of the kidney of living animals using multicolor two-photon microscopy. *American Journal of Physiology. Cell Physiology*, *283*, C905-16. https://doi.org/10.1152/ajpcell.00159.2002

Dutrochet, H., & Glasgow, U. of. (1824). *Recherches anatomiques et physiologiques sur la stricture intime des animaux et des végétaux, sur leur mobilité /* (pp. 1–618). Baillière,. https://doi.org/10.5962/bhl.title.117365

Evans, C. L., Potma, E. O., Puoris'haag, M., Côté, D., Lin, C. P., & Xie, X. S. (2005). Chemical imaging of tissue in vivo with video-rate coherent anti-Stokes Raman scattering microscopy. *Proceedings of the National Academy of Sciences*, *102*(46), 16807–16812. https://doi.org/10.1073/pnas.0508282102

Farrar, M. J., Bernstein, I. M., Schlafer, D. H., Cleland, T. A., Fetcho, J. R., & Schaffer, C. B. (2012). Chronic in vivo imaging in the mouse spinal cord using an implanted chamber. *Nature Methods*, *9*(3), 297–302. https://doi.org/10.1038/nmeth.1856

Feng, G., Mellor, R. H., Bernstein, M., Keller-Peck, C., Nguyen, Q. T., Wallace, M., Nerbonne, J. M., Lichtman, J. W., & Sanes, J. R. (2000). Imaging Neuronal Subsets in Transgenic Mice Expressing Multiple Spectral

Variants of GFP. *Neuron*, *28*(1), 41–51. https://doi.org/10.1016/S0896-6273(00)00084-2

Freudiger, C. W., Min, W., Saar, B. G., Lu, S., Holtom, G. R., He, C., Tsai, J. C., Kang, J. X., & Xie, X. S. (2008). Label-Free Biomedical Imaging with High Sensitivity by Stimulated Raman Scattering Microscopy. *Science (New York, N.Y.)*, *322*(5909), 1857–1861. https://doi.org/10.1126/science.1165758

Frith, C. (2009). Role of facial expressions in social interactions. *Philosophical Transactions of the Royal Society of London. Series B, Biological Sciences*, *364*(1535), 3453–3458. https://doi.org/10.1098/rstb.2009.0142

Fu, S. Y., & Gordon, T. (1997). The cellular and molecular basis of peripheral nerve regeneration. *Molecular Neurobiology*, *14*(1–2), 67–116. https://doi.org/10.1007/BF02740621

Gelberman, R. (1992). Operative Nerve Repair and Reconstruction. *Journal of Pediatric Orthopaedics*, *12*, 550. https://doi.org/10.1097/01241398-199207000-00038

Goldey, G. J., Roumis, D. K., Glickfeld, L. L., Kerlin, A. M., Reid, R. C., Bonin, V., Schafer, D. P., & Andermann, M. L. (2014). Long-term imaging in awake mice using removable cranial windows. *Nature Protocols*, *9*(11), 2515–2538. https://doi.org/10.1038/nprot.2014.165

Göppert-Mayer, M. (1931). Über Elementarakte mit zwei Quantensprüngen. *Annalen Der Physik*, *401*(3), 273–294. https://doi.org/10.1002/andp.19314010303

Grochmal, J., Teo, W., Gambhir, H., Kumar, R., Stratton, J. A., Dhaliwal, R., Brideau, C., Biernaskie, J., Stys, P. K., & Midha, R. (2018). A novel approach to 32-channel peripheral nervous system myelin imaging in vivo, with single axon resolution. *Journal of Neurosurgery*, *130*(1), 163–171. https://doi.org/10.3171/2017.6.JNS17239

Gutmann, E., Guttmann, L., Medawar, P. B., & Young, J. Z. (1942). The Rate of Regeneration of Nerve. *Journal of Experimental Biology*, *19*(1), 14–44.

He, Z., & Koprivica, V. (2004). The Nogo signaling pathway for regeneration block. *Annual Review of Neuroscience*, *27*, 341–368. https://doi.org/10.1146/annurev.neuro.27.070203.144340

Heaton, J. T., Sheu, S. H., Hohman, M. H., Knox, C. J., Weinberg, J. S., Kleiss, I. J., & Hadlock, T. A. (2014). Rat whisker movement after facial nerve lesion: Evidence for autonomic contraction of skeletal muscle. *Neuroscience*, *265*, 9–20. https://doi.org/10.1016/j.neuroscience.2014.01.038

Helmchen, F., & Denk, W. (2005). Deep tissue two-photon microscopy. *Nature Methods*, *2*(12), 932–940. https://doi.org/10.1038/nmeth818

Henry, F., Côté, D., Randolph, M., Rust, E., Redmond, R., Kochevar, I., Lin, C., & Winograd, J. (2009). Real-Time In Vivo Assessment of the Nerve Microenvironment with Coherent Anti–Stokes Raman Scattering Microscopy. *Plastic and Reconstructive Surgery*, *123*(2S). https://doi.org/10.1097/PRS.0b013e318191c5b8

Heo, C., Park, H., Kim, Y.-T., Baeg, E., Kim, Y. H., Kim, S.-G., & Suh, M. (2016). A soft, transparent, freely accessible cranial window for chronic imaging and electrophysiology. *Scientific Reports*, *6*, 27818. https://doi.org/10.1038/srep27818

Hill, A. H., Hill, A. H., Manifold, B., Manifold, B., & Fu, D. (2020). Tissue imaging depth limit of stimulated Raman scattering microscopy. *Biomedical Optics Express*, *11*(2), 762–774. https://doi.org/10.1364/BOE.382396

Holmquist, B., Kanje, M., Kerns, J. M., & Danielsen, N. (1993). A mathematical model for regeneration rate and initial delay following surgical repair of peripheral nerves. *Journal of Neuroscience Methods*, *48*(1–2), 27–33. https://doi.org/10.1016/s0165-0270(05)80004-4

Holtmaat, A., Bonhoeffer, T., Chow, D. K., Chuckowree, J., De Paola, V., Hofer, S. B., Hübener, M., Keck, T., Knott, G., Lee, W.-C. A., Mostany, R., Mrsic-Flogel, T. D., Nedivi, E., Portera-Cailliau, C., Svoboda, K., Trachtenberg, J. T., & Wilbrecht, L. (2009). Long-term, high-resolution imaging in the mouse neocortex through a chronic cranial window. *Nature Protocols*, *4*(8), 1128–1144. https://doi.org/10.1038/nprot.2009.89

House, J. W., & Brackmann, D. E. (1985). Facial nerve grading system. *Otolaryngology--Head and Neck Surgery: Official Journal of American Academy of Otolaryngology-Head and Neck Surgery*, *93*(2), 146–147. https://doi.org/10.1177/019459988509300202

Iadecola, C. (2004). Neurovascular regulation in the normal brain and in Alzheimer's disease. *Nature Reviews. Neuroscience*, *5*(5), 347–360. https://doi.org/10.1038/nrn1387

Ide, C., & Kato, S. (1990). Peripheral nerve regeneration. *Neuroscience Research Supplements*, *13*, S157–S164. https://doi.org/10.1016/0921-8696(90)90045-5

Ishii, L. E., Nellis, J. C., Boahene, K. D., Byrne, P., & Ishii, M. (2018). The Importance and Psychology of Facial Expression. *Otolaryngologic Clinics of North America*, *51*(6), 1011–1017. https://doi.org/10.1016/j.otc.2018.07.001

Ishii, L., Godoy, A., Encarnacion, C. O., Byrne, P. J., Boahene, K. D. O., & Ishii, M. (2012). Not just another face in the crowd: Society's perceptions of facial paralysis. *The Laryngoscope*, *122*(3), 533–538. https://doi.org/10.1002/lary.22481

Jackson, C. G., & von Doersten, P. G. (1999). THE FACIAL NERVE: Current Trends in Diagnosis, Treatment, and Rehabilitation. *Medical Clinics of North America*, *83*(1), 179–195. https://doi.org/10.1016/S0025-7125(05)70096-1

Ji, M., Orringer, D. A., Freudiger, C. W., Ramkissoon, S., Liu, X., Lau, D., Golby, A. J., Norton, I., Hayashi, M., Agar, N. Y. R., Young, G. S., Spino, C., Santagata, S., Camelo-Piragua, S., Ligon, K. L., Sagher, O., & Xie, X. S. (2013). Rapid, label-free detection of brain tumors with stimulated Raman scattering microscopy. *Science Translational Medicine*, *5*(201), 201ra119. https://doi.org/10.1126/scitranslmed.3005954

Jowett, N. (2018). A General Approach to Facial Palsy. *Otolaryngologic Clinics of North America*, *51*(6), 1019–1031. https://doi.org/10.1016/j.otc.2018.07.002

Jowett, N., & Hadlock, T. A. (2018). Free Gracilis Transfer and Static Facial Suspension for Midfacial Reanimation in Long-Standing Flaccid Facial Palsy. *Otolaryngologic Clinics of North America*, *51*(6), 1129–1139. https://doi.org/10.1016/j.otc.2018.07.009

Jung, Y., Ng, J. H., Keating, C. P., Senthil-Kumar, P., Zhao, J., Randolph, M. A., Winograd, J. M., & Evans, C. L. (2014). Comprehensive evaluation of peripheral nerve regeneration in the acute healing phase using tissue clearing and optical microscopy in a rodent model. *PloS One*, *9*(4), e94054. https://doi.org/10.1371/journal.pone.0094054

Kawakami, N., Nägerl, U. V., Odoardi, F., Bonhoeffer, T., Wekerle, H., & Flügel, A. (2005). Live imaging of effector cell trafficking and autoantigen

recognition within the unfolding autoimmune encephalomyelitis lesion. *The Journal of Experimental Medicine*, *201*(11), 1805–1814. https://doi.org/10.1084/jem.20050011

Kedrin, D., Gligorijevic, B., Wyckoff, J., Verkhusha, V. V., Condeelis, J., Segall, J. E., & van Rheenen, J. (2008). Intravital imaging of metastatic behavior through a mammary imaging window. *Nature Methods*, *5*(12), 1019–1021. https://doi.org/10.1038/nmeth.1269

Keller-Peck, C. R., Walsh, M. K., Gan, W. B., Feng, G., Sanes, J. R., & Lichtman, J. W. (2001). Asynchronous synapse elimination in neonatal motor units: Studies using GFP transgenic mice. *Neuron*, *31*(3), 381–394. https://doi.org/10.1016/s0896-6273(01)00383-x

Kienast, Y., von Baumgarten, L., Fuhrmann, M., Klinkert, W. E. F., Goldbrunner, R., Herms, J., & Winkler, F. (2010). Real-time imaging reveals the single steps of brain metastasis formation. *Nature Medicine*, *16*(1), 116–122. https://doi.org/10.1038/nm.2072

Koletar, M. M., Dorr, A., Brown, M. E., McLaurin, J., & Stefanovic, B. (2019). Refinement of a chronic cranial window implant in the rat for longitudinal in vivo two–photon fluorescence microscopy of neurovascular function. *Scientific Reports*, *9*. https://doi.org/10.1038/s41598-019-41966-9

Lee, W.-C. A., Huang, H., Feng, G., Sanes, J. R., Brown, E. N., So, P. T., & Nedivi, E. (2005). Dynamic Remodeling of Dendritic Arbors in GABAergic Interneurons of Adult Visual Cortex. *PLOS Biology*, *4*(2), e29. https://doi.org/10.1371/journal.pbio.0040029

Leeuwenhoek, A. van, & Hoole, S. (1800). *The select works of Antony van Leeuwenhoek: Containing his microscopical discoveries in many of the works of nature /* (pp. 1–364). G. Sidney,. https://doi.org/10.5962/bhl.title.5700

Légaré, F., Evans, C. L., Ganikhanov, F., & Xie, X. S. (2006). Towards CARS Endoscopy. *Optics Express*, *14*(10), 4427–4432. https://doi.org/10.1364/oe.14.004427

Lehr, H. A., Leunig, M., Menger, M. D., Nolte, D., & Messmer, K. (1993). Dorsal skinfold chamber technique for intravital microscopy in nude mice. *The American Journal of Pathology*, *143*(4), 1055–1062.

Li, M. K. K., Niles, N., Gore, S., Ebrahimi, A., McGuinness, J., & Clark, J. R. (2016). Social perception of morbidity in facial nerve paralysis. *Head & Neck*, *38*(8), 1158–1163. https://doi.org/10.1002/hed.24299

Lieberman, A. R. (1971). The axon reaction: A review of the principal features of perikaryal responses to axon injury. *International Review of Neurobiology*, *14*, 49–124. https://doi.org/10.1016/s0074-7742(08)60183-x

Lorenz, K. S., Salama, P., Dunn, K. W., & Delp, E. J. (2012). Digital Correction of Motion Artifacts in Microscopy Image Sequences Collected from Living Animals Using Rigid and Non-Rigid Registration. *Journal of Microscopy*, *245*(2). https://doi.org/10.1111/j.1365-2818.2011.03557.x

Lorimier, P., Mezin, P., Labat Moleur, F., Pinel, N., Peyrol, S., & Stoebner, P. (1992). Ultrastructural localization of the major components of the extracellular matrix in normal rat nerve. *The Journal of Histochemistry and Cytochemistry: Official Journal of the Histochemistry Society*, *40*(6), 859–868. https://doi.org/10.1177/40.6.1588030

Lundborg, G., & Rosén, B. (2007). Hand function after nerve repair. *Acta Physiologica*, *189*(2), 207–217. https://doi.org/10.1111/j.1748-1716.2006.01653.x

Lundborg, Göran. (2000). A 25-year perspective of peripheral nerve surgery: Evolving neuroscientific concepts and clinical significance. *The Journal of Hand Surgery*, *25*(3), 391–414. https://doi.org/10.1053/jhsu.2000.4165

M. D. Gelberman, R. H. (1991). *Operative Nerve Repair and Reconstruction* (First Edition edition). Lippincott Williams & Wilkins.

Macgregor, F. C. (1990). Facial disfigurement: Problems and management of social interaction and implications for mental health. *Aesthetic Plastic Surgery*, *14*(4), 249–257. https://doi.org/10.1007/bf01578358

Mackinnon, S. E., Hudson, A. R., & Hunter, D. A. (1985). Histologic assessment of nerve regeneration in the rat. *Plastic and Reconstructive Surgery*, *75*(3), 384–388. https://doi.org/10.1097/00006534-198503000-00014

McDonald, D. M., & Choyke, P. L. (2003). Imaging of angiogenesis: From microscope to clinic. *Nature Medicine*, *9*(6), 713–725. https://doi.org/10.1038/nm0603-713

Meijer, E. F. J., Jeong, H.-S., Pereira, E. R., Ruggieri, T. A., Blatter, C., Vakoc, B. J., & Padera, T. P. (2017). Murine chronic lymph node window for

longitudinal intravital lymph node imaging. *Nature Protocols*, *12*(8), 1513–1520. https://doi.org/10.1038/nprot.2017.045

Mescher, A. L. (2018). Figure Credits. In *Junqueira's Basic Histology: Text and Atlas, 15e* (Vol. 1–Book, Section). McGraw-Hill Education. accessmedicine.mhmedical.com/content.aspx?aid=1160664084

Miller, M. J., Wei, S. H., Parker, I., & Cahalan, M. D. (2002). Two-photon imaging of lymphocyte motility and antigen response in intact lymph node. *Science (New York, N.Y.)*, *296*(5574), 1869–1873. https://doi.org/10.1126/science.1070051

Millesi, H., & Terzis, J. K. (1983). Problems of terminology in peripheral nerve surgery: Committee report of the International Society of Reconstructive Microsurgery. *Microsurgery*, *4*(1), 51–56. https://doi.org/10.1002/micr.1920040113

Misgeld, T., & Kerschensteiner, M. (2006). In vivo imaging of the diseased nervous system. *Nature Reviews Neuroscience*, *7*(6), 449–463. https://doi.org/10.1038/nrn1905

Mohan, S., Coto Hernández, I., Selig, M. K., Shibata, S., & Jowett, N. (2019). Stain-Free Resolution of Unmyelinated Axons in Transgenic Mice Using Fluorescence Microscopy. *Journal of Neuropathology and Experimental Neurology*, *78*(12), 1178–1180. https://doi.org/10.1093/jnen/nlz099

Mohan, S., Hernández, I. C., Wang, W., Yin, K., Sundback, C. A., Wegst, U. G. K., & Jowett, N. (2018). Fluorescent Reporter Mice for Nerve Guidance Conduit Assessment: A High-Throughput in vivo Model. *The Laryngoscope*, *128*(11), E386–E392. https://doi.org/10.1002/lary.27439

Nellis, J. C., Ishii, M., Byrne, P. J., Boahene, K. D. O., Dey, J. K., & Ishii, L. E. (2017). Association Among Facial Paralysis, Depression, and Quality of Life in Facial Plastic Surgery Patients. *JAMA Facial Plastic Surgery*, *19*(3), 190–196. https://doi.org/10.1001/jamafacial.2016.1462

Niinomi, M. (2003). Recent research and development in titanium alloys for biomedical applications and healthcare goods. *Science and Technology of Advanced Materials*, *4*(5), 445–454. https://doi.org/10.1016/j.stam.2003.09.002

Owusu, J. A., Stewart, C. M., & Boahene, K. (2018). Facial Nerve Paralysis. *The Medical Clinics of North America*, *102*(6), 1135–1143. https://doi.org/10.1016/j.mcna.2018.06.011

Pan, F., & Gan, W.-B. (2008). Two-photon imaging of dendritic spine development in the mouse cortex. *Developmental Neurobiology*, *68*(6), 771–778. https://doi.org/10.1002/dneu.20630

Pfister, B. J., Gordon, T., Loverde, J. R., Kochar, A. S., Mackinnon, S. E., & Cullen, D. K. (2011). Biomedical engineering strategies for peripheral nerve repair: Surgical applications, state of the art, and future challenges. *Critical Reviews in Biomedical Engineering*, *39*(2), 81–124. https://doi.org/10.1615/critrevbiomedeng.v39.i2.20

Pittet, M. J., & Weissleder, R. (2011). Intravital imaging. *Cell*, *147*(5), 983–991. https://doi.org/10.1016/j.cell.2011.11.004

Porrero, C., Rubio-Garrido, P., Avendaño, C., & Clascá, F. (2010). Mapping of fluorescent protein-expressing neurons and axon pathways in adult and developing Thy1-eYFP-H transgenic mice. *Brain Research*, *1345*, 59–72. https://doi.org/10.1016/j.brainres.2010.05.061

Radtke, C., & Kocsis, J. D. (2014). Olfactory-ensheathing cell transplantation for peripheral nerve repair: Update on recent developments. *Cells, Tissues, Organs*, *200*(1), 48–58. https://doi.org/10.1159/000369006

Ray, W. Z., & Mackinnon, S. E. (2010). Management of nerve gaps: Autografts, allografts, nerve transfers, and end-to-side neurorrhaphy. *Experimental Neurology*, *223*(1), 77–85. https://doi.org/10.1016/j.expneurol.2009.03.031

Ritsma, L., Steller, E. J. A., Ellenbroek, S. I. J., Kranenburg, O., Borel Rinkes, I. H. M., & van Rheenen, J. (2013). Surgical implantation of an abdominal imaging window for intravital microscopy. *Nature Protocols*, *8*(3), 583–594. https://doi.org/10.1038/nprot.2013.026

Rydevik, B. L., Kwan, M. K., Myers, R. R., Brown, R. A., Triggs, K. J., Woo, S. L.-Y., & Garfin, S. R. (1990). An in vitro mechanical and histological study of acute stretching on rabbit tibial nerve. *Journal of Orthopaedic Research*, *8*(5), 694–701. https://doi.org/10.1002/jor.1100080511

Ryzenman, J. M., Pensak, M. L., & Tew, J. M. (2005). Facial paralysis and surgical rehabilitation: A quality of life analysis in a cohort of 1,595 patients after acoustic neuroma surgery. *Otology & Neurotology: Official Publication of the American Otological Society, American Neurotology Society [and] European Academy of Otology and Neurotology*, *26*(3), 516–521; discussion 521. https://doi.org/10.1097/01.mao.0000169786.22707.12

Salonen, V., Lehto, M., Vaheri, A., Aro, H., & Peltonen, J. (1985). Endoneurial fibrosis following nerve transection. *Acta Neuropathologica*, *67*(3), 315–321. https://doi.org/10.1007/BF00687818

Scheib, J., & Höke, A. (2013). Advances in peripheral nerve regeneration. *Nature Reviews. Neurology*, *9*(12), 668–676. https://doi.org/10.1038/nrneurol.2013.227

Seddon, H. J. (1943). THREE TYPES OF NERVE INJURY. *Brain*, *66*(4), 237–288. https://doi.org/10.1093/brain/66.4.237

Sharma, A. K., Bajada, S., & Thomas, P. K. (1980). Age changes in the tibial and plantar nerves of the rat. *Journal of Anatomy*, *130*(Pt 2), 417–428.

Shibata, S., Yasuda, A., Renault-Mihara, F., Suyama, S., Katoh, H., Inoue, T., Inoue, Y. U., Nagoshi, N., Sato, M., Nakamura, M., Akazawa, C., & Okano, H. (2010). Sox10-Venus mice: A new tool for real-time labeling of neural crest lineage cells and oligodendrocytes. *Molecular Brain*, *3*, 31. https://doi.org/10.1186/1756-6606-3-31

Shimozawa, A. (1976). Quantitative studies on the mouse facial nerve trunk distal to the geniculate ganglion. An electron-microscopic study. *Acta Anatomica*, *95*(4), 529–536. https://doi.org/10.1159/000144640

So, P. T. C., Dong, C. Y., Masters, B. R., & Berland, K. M. (2000). Two-Photon Excitation Fluorescence Microscopy. *Annual Review of Biomedical Engineering*, *2*(1), 399–429. https://doi.org/10.1146/annurev.bioeng.2.1.399

Squirrell, J. M., Wokosin, D. L., White, J. G., & Bavister, B. D. (1999). Long-term two-photon fluorescence imaging of mammalian embryos without compromising viability. *Nature Biotechnology*, *17*(8), 763–767. https://doi.org/10.1038/11698

Standring, S., & Gray, H. (2008). *Gray's anatomy: The anatomical basis of clinical practice.*

Sunderland, S., Sydney. (1978). *Nerves and nerve injuries* (2d ed). Edinburgh ; New York : Churchill Livingstone ; New York : distributed by Longman. https://trove.nla.gov.au/version/45238706

Svoboda, K., Tank, D. W., & Denk, W. (1996). Direct measurement of coupling between dendritic spines and shafts. *Science (New York, N.Y.)*, *272*(5262), 716–719. https://doi.org/10.1126/science.272.5262.716

te Velde, E. A., Wagenaar, G. T. M., Reijerkerk, A., Roose-Girma, M., Borel Rinkes, I. H. M., Voest, E. E., Bouma, B. N., Gebbink, M. F. B. G., & Meijers, J. C. M. (2003). Impaired healing of cutaneous wounds and colonic anastomoses in mice lacking thrombin-activatable fibrinolysis inhibitor. *Journal of Thrombosis and Haemostasis: JTH*, *1*(10), 2087–2096. https://doi.org/10.1046/j.1538-7836.2003.00404.x

Thomas M. Brushart, M. D. (n.d.). *Nerve Repair*. Oxford University Press. Retrieved December 16, 2019, from https://oxfordmedicine.com/view/10.1093/med/9780195169904.001.0001/med-9780195169904

Thomas, P. K. (1963). The connective tissue of peripheral nerve: An electron microscope study. *Journal of Anatomy*, *97*, 35–44.

Tian, F., Yang, W., Mordes, D. A., Wang, J.-Y., Salameh, J. S., Mok, J., Chew, J., Sharma, A., Leno-Duran, E., Suzuki-Uematsu, S., Suzuki, N., Han, S. S., Lu, F.-K., Ji, M., Zhang, R., Liu, Y., Strominger, J., Shneider, N. A., Petrucelli, L., … Eggan, K. (2016). Monitoring peripheral nerve degeneration in ALS by label-free stimulated Raman scattering imaging. *Nature Communications*, *7*, 13283. https://doi.org/10.1038/ncomms13283

Vargas, M. E., & Barres, B. A. (2007). Why is Wallerian degeneration in the CNS so slow? *Annual Review of Neuroscience*, *30*, 153–179. https://doi.org/10.1146/annurev.neuro.30.051606.094354

Wang, H., Huff, T. B., Fu, Y., Jia, K. Y., & Cheng, J.-X. (2007). Increasing the imaging depth of coherent anti-Stokes Raman scattering microscopy with a miniature microscope objective. *Optics Letters*, *32*(15), 2212–2214. https://doi.org/10.1364/OL.32.002212

Wang, Weigang, Wyckoff, J. B., Frohlich, V. C., Oleynikov, Y., Hüttelmaier, S., Zavadil, J., Cermak, L., Bottinger, E. P., Singer, R. H., White, J. G., Segall, J. E., & Condeelis, J. S. (2002). Single cell behavior in metastatic primary mammary tumors correlated with gene expression patterns revealed by molecular profiling. *Cancer Research*, *62*(21), 6278–6288.

Wang, Wenjin, Kang, S., Coto Hernández, I., & Jowett, N. (2019). A Rapid Protocol for Intraoperative Assessment of Peripheral Nerve Myelinated Axon Count and Its Application to Cross-Facial Nerve Grafting. *Plastic and*

Reconstructive Surgery, *143*(3), 771–778. https://doi.org/10.1097/PRS.0000000000005338

Wei, L., Yu, Y., Shen, Y., Wang, M. C., & Min, W. (2013). Vibrational imaging of newly synthesized proteins in live cells by stimulated Raman scattering microscopy. *Proceedings of the National Academy of Sciences*, *110*(28), 11226–11231. https://doi.org/10.1073/pnas.1303768110

Wei, M., Shi, L., Shen, Y., Zhao, Z., Guzman, A., Kaufman, L. J., Wei, L., & Min, W. (2019). Volumetric chemical imaging by clearing-enhanced stimulated Raman scattering microscopy. *Proceedings of the National Academy of Sciences*, *116*(14), 6608–6617. https://doi.org/10.1073/pnas.1813044116

Wood, M. D., Kemp, S. W. P., Weber, C., Borschel, G. H., & Gordon, T. (2011). Outcome measures of peripheral nerve regeneration. *Annals of Anatomy = Anatomischer Anzeiger: Official Organ of the Anatomische Gesellschaft*, *193*(4), 321–333. https://doi.org/10.1016/j.aanat.2011.04.008

Wright, A. J., Poland, S. P., Girkin, J. M., Freudiger, C. W., Evans, C. L., & Xie, X. S. (2007). Adaptive optics for enhanced signal in CARS microscopy. *Optics Express*, *15*(26), 18209–18219. https://doi.org/10.1364/OE.15.018209

Zhang, X., Roeffaers, M. B. J., Basu, S., Daniele, J. R., Fu, D., Freudiger, C. W., Holtom, G. R., & Xie, X. S. (2012). Label-free live-cell imaging of nucleic acids using stimulated Raman scattering microscopy. *Chemphyschem: A European Journal of Chemical Physics and Physical Chemistry*, *13*(4), 1054–1059. https://doi.org/10.1002/cphc.201100890

Zipfel, W. R., Williams, R. M., & Webb, W. W. (2003). Nonlinear magic: Multiphoton microscopy in the biosciences. *Nature Biotechnology*, *21*(11), 1369–1377. https://doi.org/10.1038/nbt899

CURRICULUM VITAE